

Studies for a Photon Collider at the ILC

F. Bechtel^a G. Klämke^{a,b} G. Klemz^{a,c} K. Mönig^{a,*} H. Nieto^a
H. Nowak^a A. Rosca^{a,d} J. Sekaric^{a,e} A. Stahl^{a,f}

^a*DESY, Zeuthen, Germany*

^b*now at Inst. für Theo. Phys., Uni. Karlsruhe, Germany*

^c*now at Max Born Inst., Berlin, Germany*

^d*now at West Uni. of Timisoara, Romania*

^e*now at Florida State Univ., Tallahassee, USA*

^f*now at III. Phys. Inst., RWTH Aachen, Germany*

Abstract

One option at the International Linear Collider is to convert the electron beams into high energy photon beams by Compton scattering a few millimetres in front of the interaction region. Selected physics channels for this option have been analysed and technical issues have been studied. So far no showstoppers for this option have been found.

1 Introduction

Collisions between photons are interesting in many respects. Up to now they could only be realised in e^+e^- colliders as collisions between virtual or quasi-real photons radiated off the electrons. This had the big disadvantage that the photon energy on average is much lower than the energy of the electrons.

Contrary to a storage ring, in an e^+e^- linear collider the beams collide only once. It should thus be possible to convert the electrons into high energy photons by scattering them on a high power laser a few mm in front of the interaction point [1]. If the laser wavelength is chosen correctly photon energies up to 80% of the electron beam energy can be achieved.

* Corresponding author, email: Klaus.Moenig@desy.de

There are several reasons why a photon collider is interesting for particle physics [2]. Photons couple equally to all charged particles. Since there are no interferences involved in the process and the particles are produced via t-channel exchange the cross sections are in most cases significantly larger than in e^+e^- . In most cases these cross sections are just given by the charge of the produced particles and phase space factors. This makes the production less interesting than in e^+e^- , where the non-trivial weak couplings of the particles can be measured. However, the large and model independent cross section offers an excellent possibility to study the decays of the produced particles. In the case of W-production their gauge couplings can be measured, where $\gamma\gamma \rightarrow W^+W^-$ is only sensitive to the photon couplings of the W without uncertainties from the Z. Neutral particles can couple to photons only via loops. The particles running in the loops can be too heavy to be produced at the collider, but their effect can be measured from the production cross section of a neutral particle. The production of Higgs bosons is very interesting in this respect, since the coupling of the Higgses to photons is sensitive to all charged particles that receive their mass from the Higgs mechanism and for example in SUSY models also to their superpartners.

In addition to the $\gamma\gamma$ mode a photon collider can also be used as an $e\gamma$ collider. There is a significant $e\gamma$ luminosity in the $\gamma\gamma$ mode due to unconverted electrons, denoted as parasitic $e\gamma$ mode in the following. If needed, also only one beam can be converted to get a larger $e\gamma$ luminosity with less background.

The detailed layout of a photon collider depends on the parameters of the linear accelerator. Especially the time structure of the beam influences directly the layout of the laser system. In this paper the layout of the TESLA machine [3] will be used. The design of the ILC is not yet finalised, but the time structure will be very similar to the ones studied for TESLA [4]. A principle layout of a photon collider at TESLA is presented in [2].

1.1 Principles of a Photon Collider

1.1.1 Compton scattering

The high energy photons at a photon collider are produced by Compton scattering of a high energy electron beam with a high power laser. From pure kinematics the maximum photon energy ω_m is given by

$$\omega_m = \frac{x}{x+1} E_0$$

with E_0 being the beam energy and

$$x = \frac{4E_0\omega_0}{m_e^2 c^4} \cos^2 \frac{\alpha_l}{2} \simeq 19 \left[\frac{E_0}{\text{TeV}} \right] \left[\frac{\mu\text{m}}{\lambda} \right].$$

ω_0 and λ denote the photon energy and wavelength of the laser and α_l denotes the crossing angle between the laser and the electron beam. In the approximation the assumption $\cos \alpha_l/2 = 1$ is used which is always fulfilled in praxis. It is desirable to keep x below 4.8, since for larger x the invariant mass between a high energy photon and a laser photon is above the e^+e^- pair production threshold, so that the high energy photons are lost again due their interaction with the laser. The most powerful solid state lasers have a wavelength around $\lambda \approx 1\mu\text{m}$ resulting in $x = 4.75$ for a 250 GeV beam.

The differential cross section with respect to the photon energy ω_0 for Compton scattering is given by [2]:

$$\frac{d\sigma_c}{dy} = \frac{2\sigma_0}{x} \left[\frac{1}{1-y} + 1 - y - 4r(1-r) + 2\lambda_e P_c r x (1-2r)(2-y) \right]$$

with $y = \omega_0/E_0$, $r = \frac{y}{(1-y)x}$ and $\sigma_0 = \pi r_e^2$. The cross section is strongly sensitive to the product of the electron helicity λ_e and the laser circular polarisation P_c . The left plot of figure 1 shows the normalised cross section for different values of $2\lambda_e P_c$. A value close to -1 should be used to obtain maximum luminosity at high energies.

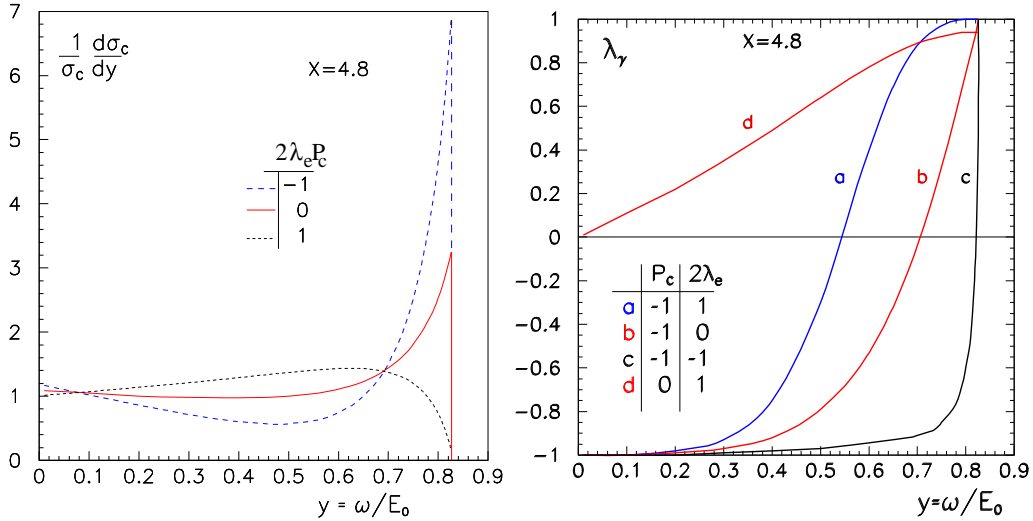


Figure 1. Left: normalised photon energy energy spectrum from Compton scattering for different electron and laser polarisation; right: photon circular polarisation for different electron and laser polarisation.

The helicity of the final state photons is given by

$$\langle \lambda_\gamma \rangle = \frac{-P_c(2r-1)[(1-y)^{-1} + 1-y] + 2\lambda_e x r[1 + (1-y)(2r-1)^2]}{(1-y)^{-1} + 1-y - 4r(1-r) - 2\lambda_e P_c x r(2-y)(2r-1)}$$

The right plot of figure 1 shows the photon helicity for different values of the electron and laser polarisation. $2\lambda_e P_c = -1$ results in a high and relatively constant polarisation in the high energy peak with a strong variation at lower energies.

The photon spectrum in a real collider is more complicated than the one given from pure Compton scattering for two reasons. The Compton cross section rises for smaller centre of mass energies. The electrons that have interacted once have thus a high chance to interact a second time giving rise to a much enhanced spectrum at low photon energies. In addition the laser power is so high that non-linear effects have to be taken into account [5,6,7,8]. They can be parametrised by the parameter

$$\xi^2 = \frac{e^2 \bar{F}^2 \hbar^2}{m^2 c^2 \omega_0^2} = \frac{2n_\gamma r_e^2 \lambda}{\alpha}$$

where \bar{F} denotes the field strength of the laser field and n_γ the corresponding photon density. The non-linear effects modify the photon spectrum in two ways. The effective electron mass increases by a factor $(1 + \xi^2)$ reducing the maximum energy to $\omega_m/E_0 = x/(1 + x + \xi^2)$. At the same time a high energy tail develops due to the simultaneous interaction of one electron with several laser photons. Figure 2 shows the photon energy spectrum for different ξ^2 .

For the calculation of the luminosity spectrum one has to take into account that lower energy photons are produced at larger angles with respect to the original beam direction so that their luminous spot is larger, reducing the luminosity for low centre of mass energies. To calculate the photon spectrum in a real collider, simulation programs have to be used. In this paper the program CAIN [9] is used which calculates the beam-laser as well as the beam-beam interaction taking non-linearity and beam polarisation effects into account. Figure 3 shows the $\gamma\gamma$ centre of mass energy spectrum and polarisation for the chosen laser parameters and $\sqrt{s_{ee}} = 500$ GeV.

1.1.2 Machine Parameters

A photon collider will be operated with two electron beams instead of an electron and a positron beam for several reasons. Electrons can be polarised to a higher degree than positrons resulting in a more favourable luminosity spectrum. Two electron beams defocus each other in the interaction point generat-

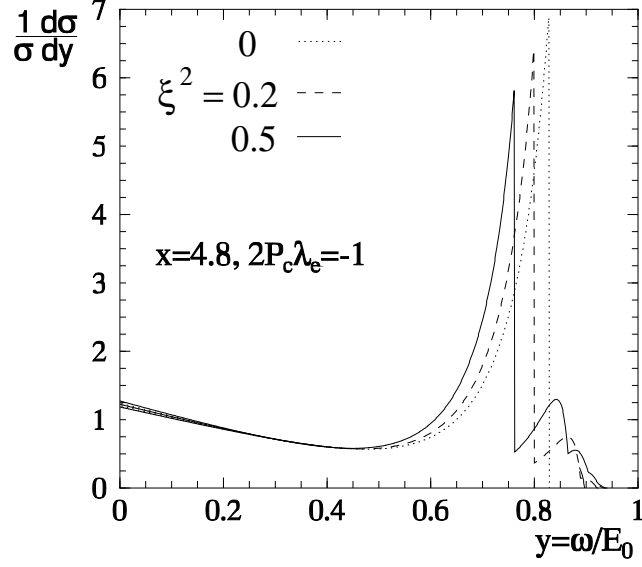


Figure 2. Normalised photon energy spectrum from Compton scattering for different nonlinearity parameters [2].

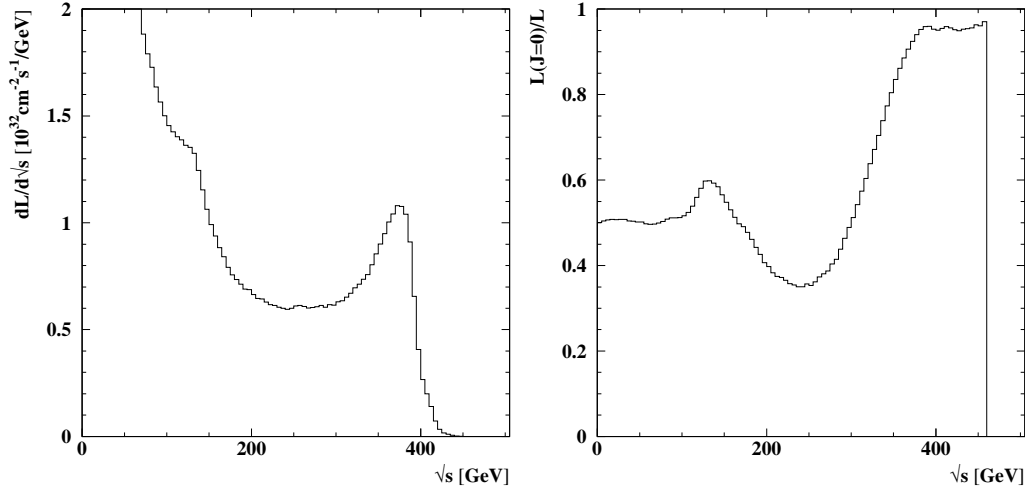


Figure 3. Luminosity spectrum (left) and fraction of $J=0$ luminosity (right) from CAIN for $\sqrt{s}_{ee} = 500$ GeV. The beam parameters labelled “ $\gamma\gamma$ [2]” from table 1 and the laser parameters from table 5 have been used.

ing less beamstrahlung than electron-positron interactions. Electron-electron interactions result in no annihilation events which would be a background for the high energy $\gamma\gamma$ interactions. Since the beamstrahlung for identical beam parameters is smaller at the $\gamma\gamma$ collider than in the e^+e^- case, the beams can be focused stronger resulting in a higher luminosity. Table 1 compares a set of conservative [3] and optimistic [2] parameters with the ones of the e^+e^- collider [3] for a beam energy of 250 GeV. For the optimistic set a third of the e^+e^- luminosity can be obtained in the high energy part of the spectrum. Since the optimistic set results in higher backgrounds it will be used consistently in this paper. To reach the same physics results with the more

conservative set the running time has to be doubled. The total luminosity with the optimistic design is around $\mathcal{L} = 10^{35} \text{cm}^{-2} \text{s}^{-1}$, where about 10% are in the interesting high energy region. In the physics studies presented in section 2, it will be assumed that a year of running corresponds to 10^7 seconds at design luminosity.

Figure 4 shows the $e\gamma$ luminosity for the $\gamma\gamma$ and for the $e\gamma$ collider at $\sqrt{s}_{ee} = 500 \text{ GeV}$, where only one beam is converted and all other parameters are left identical to the $\gamma\gamma$ collider. The $e\gamma$ luminosity in the high energy part of the spectrum ($\sqrt{s}_{e\gamma} > 360 \text{ GeV}$) is $\mathcal{L} = 1.3 \cdot 10^{34} \text{cm}^{-2} \text{s}^{-1}$ for the $\gamma\gamma$ collider and $\mathcal{L} = 2.4 \cdot 10^{34} \text{cm}^{-2} \text{s}^{-1}$ for the $e\gamma$ collider.

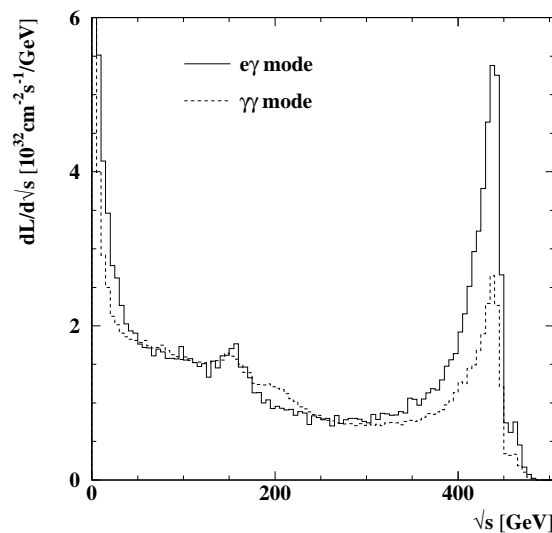


Figure 4. Differential $e\gamma$ luminosity for the egm - (solid) and $\gamma\gamma$ -collider (dashed) at $\sqrt{s}_{ee} = 500 \text{ GeV}$.

Table 1

Beam parameters for the e^+e^- and the $\gamma\gamma$ collider for $E_b = 250 \text{ GeV}$.

	e^+e^- [3]	$\gamma\gamma$ [3]	$\gamma\gamma$ [2]
$N/10^{10}$	2	2	2
σ_z [mm]	0.3	0.3	0.3
pulses/train	2820	2820	2820
Repetition rate [Hz]	5	5	5
$\gamma\epsilon_{x/y}/10^{-6}$ [m·rad]	10./0.03	3./0.03	2.5/0.03
$\beta_{x/y}$ [mm] at IP	15/0.4	4/0.4	1.5/0.3
$\sigma_{x/y}$ [nm]	553/5	157/5	88/4.3
$\mathcal{L}(z > 0.8z_m)$ [$10^{34} \text{cm}^{-2} \text{s}^{-1}$]	3.4	0.6	1.1

For parity conserving processes only the total $\gamma\gamma$ and $e\gamma$ angular momentum

matters. The available states are $|J_z| = 0, 2$ for $\gamma\gamma$ and $|J_z| = 1/2, 3/2$ for $e\gamma$ ¹. For studies of CP violation in $\gamma\gamma$ the two $J_z = 0$ states $\lambda_\gamma = (1, 1)$ and $\lambda_\gamma = (-1, -1)$ give different information, while the two states $J_z = \pm 2$ follow from each other by a rotation of the coordinate system. Weak processes violate parity, especially the W couples only to left-handed fermions. For this reason the sign of J_z is important for many processes in $e\gamma$.

Because of the large disruption of the electron beam in the interaction with the laser the spent beam cannot leave the detector through the hole of the incoming one which is limited by the aperture of the final quadrupole. For this reason a crossing angle is needed. The exact value depends on the size of the final focus quadrupole. This study assumes a value of $\alpha = 35$ mrad, however with recent quadrupole designs [10] a smaller angle seems possible.

1.1.3 Beam simulation

For the simulation of the laser-beam and beam-beam interactions many effects must be taken into account. In the laser-beam interaction non-linear effects are important where the non-linearity varies with space and time and particles can interact several times before they leave the interaction region. In the beam-beam interactions apart from the interesting high-energy events one has to consider coherent effects of a particle from one bunch interacting with the coherent field of the opposing bunch, so called beamstrahlung, and incoherent interactions of single particles from the two bunches. In addition all processes can influence the polarisation of the particles.

All processes are included in the simulation program CAIN [9] which has been used throughout this paper. Where possible CAIN has been checked against GuineaPig [11] and the program of V. Telnov [12]. Reasonable agreement has been found in all cases when a comparison is possible.

For physics studies the beam simulations are not appropriate and fast programs have been developed which generate the interacting beam particles and have been tuned to the beam simulation programs. For the studies presented in this paper the programs CIRCE2 [13], based on a histogramming technique, and CompAZ [14], based on analytic parameterisations, have been used.

¹ In the following J_z always denotes the total angular momentum for the high energy part of the spectrum.

2 The Physics Case for a $\gamma\gamma$ Collider

Photons couple to all charged particles and via loops also to neutral particles like the Higgs. The pair production of charged particles proceeds via t-channel exchange where the energy suppression in the propagator is smaller than for s-channel production. The typical cross sections in $\gamma\gamma$ are thus significantly larger than in e^+e^- . The couplings of photons to charged particles are also well known so that the cross section can be calculated reliably, contrary to e^+e^- , where the production normally proceeds via photon and Z exchange, where both amplitudes and their relative phase need to be known. On one hand this makes the production cross section in $\gamma\gamma$ much less interesting than in e^+e^- . On the other hand the large samples can be used to learn about the decay properties of the produced particles. Figure 5 compares the production cross section of several particles in e^+e^- , $e\gamma$ and $\gamma\gamma$ [15].

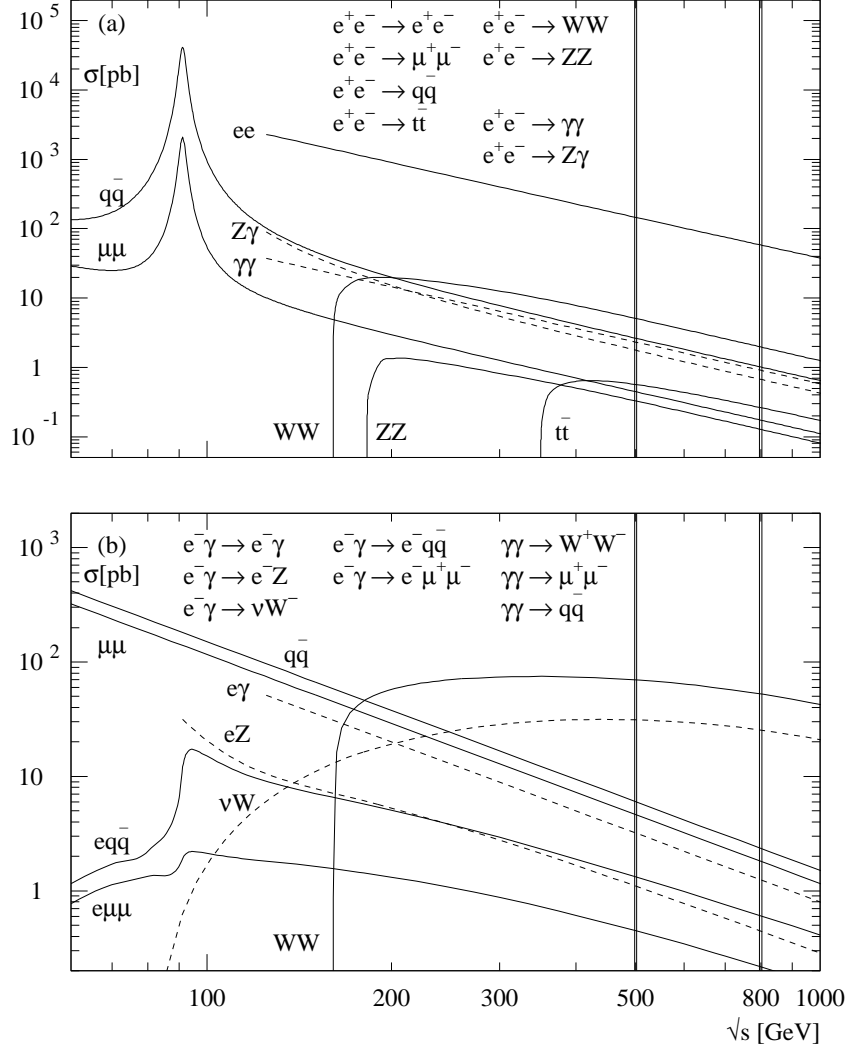


Figure 5. Cross section for some processes in e^+e^- , $e\gamma$ and $\gamma\gamma$.

The physics case of the $\gamma\gamma$ collider is largely complementary to e^+e^- [16]. While in $\gamma\gamma$ the decays can be studied e^+e^- measured the production mechanism in great detail.

A summary of interesting physics channels can be found in [2,17]. In the following a few examples that are of special interest in the motivation of the $\gamma\gamma$ collider will be discussed.

2.1 Pileup

The cross section $\gamma\gamma \rightarrow \text{hadrons}$ is several hundred nb, relatively independent on the centre of mass energy [18]. The total $\gamma\gamma$ luminosity is $\mathcal{L} = 1.0 \cdot 10^{35} \text{cm}^{-2}\text{s}^{-1}$ mainly concentrated at low centre of mass energy (see Fig. 3), corresponding to several μb^{-1} per bunch crossing. This leads to one to two $\gamma\gamma \rightarrow \text{hadrons}$ events per bunch crossing, depending on the centre of mass energy, $\sqrt{s_{ee}}$, and running mode, that overlay the physics events of interest (pileup). In the physics studies these events are taken from a database [19] and added to the physics events with the right frequency. For the 337 ns bunch spacing at TESLA the bunch crossing can be tagged unambiguously for every track so that only single bunch crossings need to be considered.

Since the $\gamma\gamma \rightarrow \text{hadrons}$ events are induced by quark t-channel exchange and have on average a rather large boost in one direction most tracks are concentrated at low angles (Fig. 6). For analyses of channels where most particles are in the central region, like $\gamma\gamma \rightarrow H$ a large part of the pileup can be rejected by a simple cut on the polar angle.

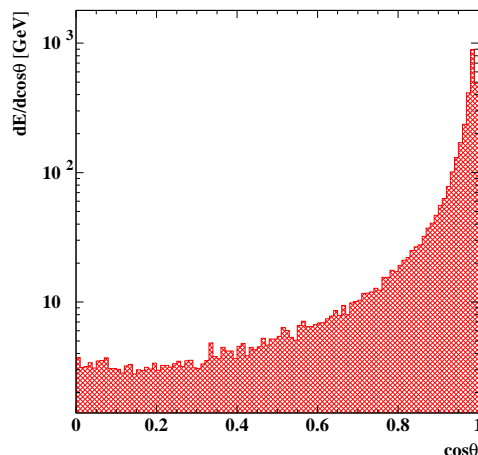


Figure 6. Polar angle distribution for pileup tracks.

The bunch length at TESLA is $\sigma_z \approx 300 \mu\text{m}$ leading to a beamspot length of $200 \mu\text{m}$. This is much larger than the impact parameter resolution of the microvertex detector which is around $5 \mu\text{m}$ for large momenta. The measure-

ment of the impact parameter of a particle along the beam axis with respect to the primary vertex can thus also be used to separate tracks from the high energy signal and the pileup. Fig. 7 shows the impact parameter in z divided by its error for tracks from $\gamma\gamma \rightarrow W^+W^-$ and from pileup and the efficiency for a cut in this variable. For a loss of only 5-10% of the signal tracks about half of the tracks from pileup can be rejected. If enough tracks to reconstruct the primary vertex are in the central part of the detector and only tracks in this region need to be considered for the analysis 85% of the pileup tracks can be rejected with only a 1% loss of signal tracks. This analysis was done for a channel without b-quarks in the events. In this case the primary vertex can simply be calculated as the mean momentum weighted z -impact parameter². In events with a large b-quark contents like Higgs production similar results are expected, however a more sophisticated vertex reconstruction is needed.

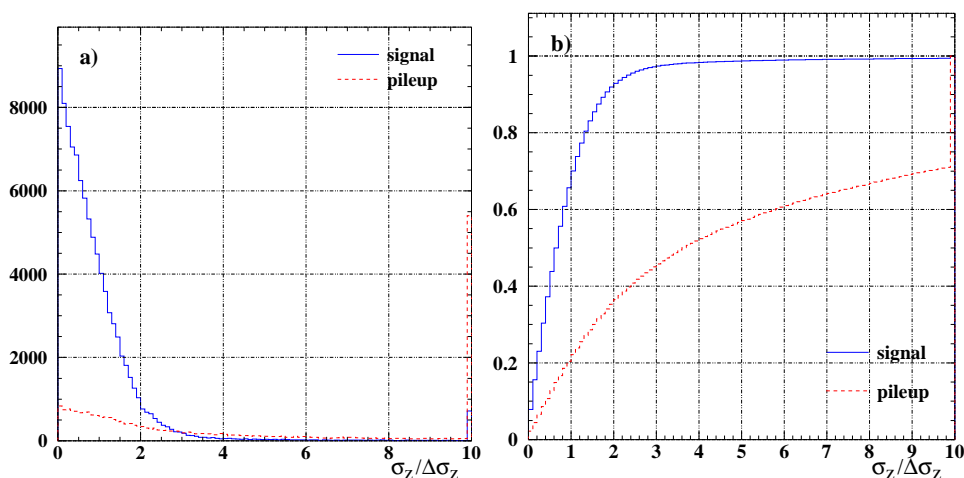


Figure 7. a) Normalised z -impact parameter distribution for signal and pileup tracks. b) Track tagging efficiency for a cut on the normalised z -impact parameter for signal and pileup tracks.

For physics, where the tracks are peaked in the forward region, like the production of W -bosons, the pileup events are a severe problem. In addition the pileup contributes roughly 15 hits per layer in the microvertex detector. This dominates over the hits from beam beam interactions in the outer three layers

2.2 Higgs

In the framework of the standard model, the generation of mass of both fermions and gauge bosons occurs through interactions with the same scalar particle, the Higgs boson. By the time a Photon Collider is constructed the Higgs boson will certainly be discovered. Therefore the aim of this machine

² The z -impact parameter is defined as the z -coordinate of the impact point in the x - y plane

will be a precise measurement of its properties, as for instance a high precision measurement of the $h \rightarrow \gamma\gamma$ partial width. The measurement of this quantity offers an indirect signature for physics beyond the standard model in case a deviation from the standard model will be found.

At a Photon Collider one can measure the product $\Gamma(h \rightarrow \gamma\gamma) \times \text{BR}(h \rightarrow X)$. When this measurement is combined with the measurement of the $\text{BR}(h \rightarrow X)$ from e^+e^- running one can obtain the partial width independent of the branching ratio.

In this study the process $\gamma\gamma \rightarrow h \rightarrow b\bar{b}$ has been studied in detail assuming $m_h = 120$ GeV. The feasibility of this measurement in the intermediate mass region has also been reported by [20,21,22,23].

2.2.1 Simulation of the signal and background processes

For the Higgs study a total angular momentum of $J_z = 0$ is used. In this case the cross sections for the direct continuum $\gamma\gamma \rightarrow b\bar{b}$ and $\gamma\gamma \rightarrow c\bar{c}$ production, the main background processes, are suppressed by a factor $M_q^2/s_{\gamma\gamma}$, with M_q being the quark mass.

The beam spectra at $\sqrt{s_{ee}} = 210$ GeV are simulated using the CompAZ [14] parameterisation. The response of the detector has been simulated with SIMDET 4 [24], a parametric Monte Carlo for the TESLA e^+e^- detector. The only difference between this detector and a Photon Collider detector is the acceptance of the latter one which is simulated taking for the Higgs reconstruction only the energy-flow-objects reconstructed with a polar angle above 7° .

Signal $\gamma\gamma \rightarrow h \rightarrow b\bar{b}$ events are generated using PYTHIA 6.2 [25]. Background processes $\gamma\gamma \rightarrow q\bar{q}(g)$ are generated with the SHERPA [26] generator. A detailed description of the simulation of the background processes with SHERPA can be found in Reference [27].

For $\sqrt{s_{ee}} = 210$ GeV about one pileup event per bunch crossing has to be taken into account. A large fraction of this background is distributed at small angles and it is reduced requiring the cosine of the polar angle of the energy-flow-objects to be below 0.95.

2.2.2 Event selection and results

The selection of the events originating from the $\gamma\gamma \rightarrow h \rightarrow b\bar{b}$ is described in Reference [28]. Events which contain two or three jets are selected. Jet are reconstructed using the DURHAM [29] algorithm. The invariant mass of the jets has to be consistent with the Higgs mass and two of the jets must be

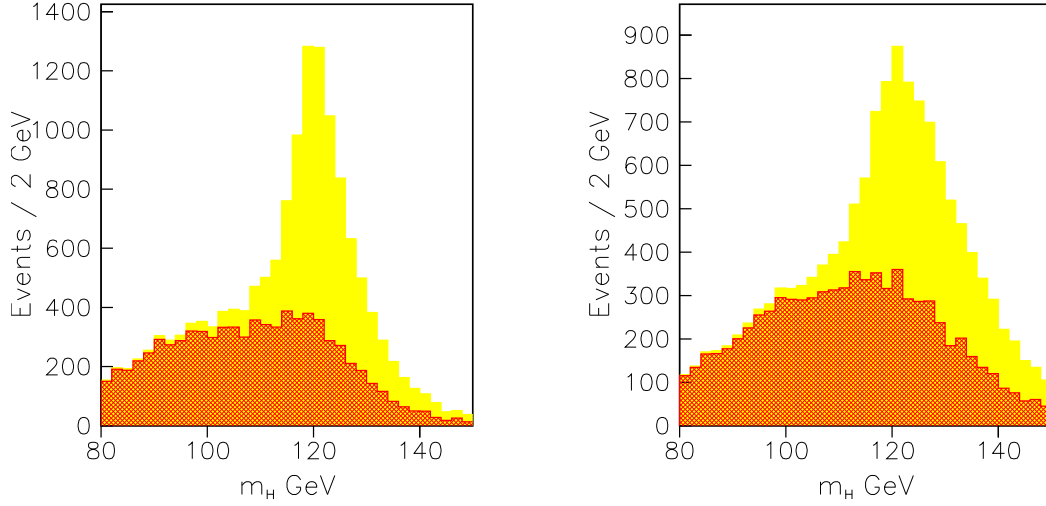


Figure 8. Distribution of the reconstructed invariant mass for the signal and background events.

produced by the hadronisation of bottom quarks.

Typical selection variables are: the visible energy of the event; the longitudinal imbalance in the event, the cosine of the thrust angle and the output of the Neural Network [30] for tagging bottom quarks for the fastest two energetic jets in the event.

The reconstructed invariant mass for the selected signal and background processes is shown in Figure 8a if no pileup is overlaid and in Figure 8b when 1 pileup event is considered per bunch crossing. To enhance the signal a cut on the invariant mass is tuned such that the statistical significance of the signal over background is maximised. Events in the mass region of $116 \text{ GeV} < M_{jj} < 132 \text{ GeV}$ are selected. The number of estimated signal and background events in this window are 3676 and 2317, respectively.

The two photon decay width of the Higgs boson is proportional to the event rates of the Higgs signal. The statistical error of the number of signal events, $\sqrt{N_{\text{obs}}}/(N_{\text{obs}} - N_{\text{bkg}})$, corresponds to the statistical error of this measurement. Here N_{obs} is the number of observed events, while N_{bkg} is the number of expected background events.

$$\frac{\Delta[\Gamma(h \rightarrow \gamma\gamma) \times \text{BR}(h \rightarrow b\bar{b})]}{[\Gamma(h \rightarrow \gamma\gamma) \times \text{BR}(h \rightarrow b\bar{b})]} = \sqrt{N_{\text{obs}}}/(N_{\text{obs}} - N_{\text{bkg}}) = 2.1\%$$

can be obtained. For a Higgs boson with a mass $M_H=120 \text{ GeV}$ the product $\Gamma(H \rightarrow \gamma\gamma) \times \text{BR}(H \rightarrow b\bar{b})$ can thus be measured with an accuracy of 2.1% using an integrated luminosity corresponding to one year of data taking at the TESLA Photon Collider of 80 fb^{-1} in the high energy part of the spectrum.

2.3 Gauge Boson Couplings

The triple gauge boson couplings $WW\gamma$ can be measured in the processes $e\gamma \rightarrow W\nu$ and $\gamma\gamma \rightarrow W^+W^-$. Both processes have a large cross section, ~ 35 pb for $e\gamma$ and ~ 80 pb for $\gamma\gamma$ and unpolarised beams. The contributing Feynman diagrams are shown in figure 9. In the $\gamma\gamma$ process the only contributing diagram contains the triple gauge coupling. In the $e\gamma$ process the electron t-channel exchange can be switched off if $|J_z| = 3/2$ is used. The cross sections are about an order of magnitude larger than in e^+e^- , however the sensitivity to the triple gauge couplings is not enhanced by gauge cancellations.

The C and P conserving couplings κ_γ and λ_γ [31,32] have been analysed in both processes [33,34]. Since in both cases the beam energy varies and in addition there is a missing neutrino in $e\gamma$, a neutrino from a W decay cannot be reconstructed from the missing four-momentum, only hadronic W-decays have been used in the analysis. However this is by far not such a large problem as in e^+e^- since there is no need to separate the W^+ from the W^- . Only the sign of the W-helicity cannot be measured in this case.

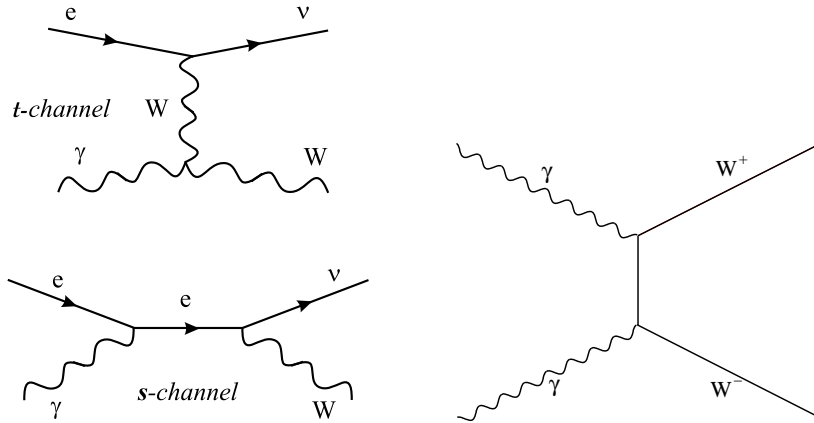


Figure 9. Feynman diagrams for $e\gamma \rightarrow W\nu$ (left) and $\gamma\gamma \rightarrow W^+W^-$ (right).

2.3.1 Analysis of $e\gamma \rightarrow W\nu$

In the $e\gamma$ case the “real mode”, where only one electron beam is converted into photons, and the “parasitic mode”, where both beams are converted and the $e\gamma$ luminosity of the unconverted electrons is used, have been analysed [33]. Possible backgrounds in the real mode are the $\gamma\gamma$ induced process $e\gamma \rightarrow eq\bar{q}$ and $e\gamma \rightarrow eZ$ where the electron is lost in the forward region. In the parasitic mode in addition $\gamma\gamma \rightarrow q\bar{q}$ and $\gamma\gamma \rightarrow W^+W^-$ where one W decays leptonically and the charged lepton is lost, have to be considered.

In the analysis the electron beam always has been assumed to be dominantly left-handed and the $e\gamma$ angular momentum is set to $|J_z| = 3/2$.

In a first step of the analysis pileup tracks are rejected. Tracks are rejected if their z-impact parameter is inconsistent with the primary vertex. In addition tracks are rejected if they are far away from the reconstructed W-axis where the cut is stronger if the tracks are in the forward region. Figure 10 shows the reconstructed W mass and energy distribution using all tracks, the tracks that pass the impact parameter cut and the tracks that pass in addition the angle cuts. The large tails get reduced significantly by the cuts for the price of a worse mass resolution. In a second step events are selected by a cut on the reconstructed mass and energy of the W. These cuts result in an efficiency of 73% (66%) with a purity of 64% (49%) in the real (parasitic) mode. The background is extremely forward peaked and an additional cut of $\theta_W > 5^\circ$ results in a purity of 95% (72%) basically without a loss in efficiency.

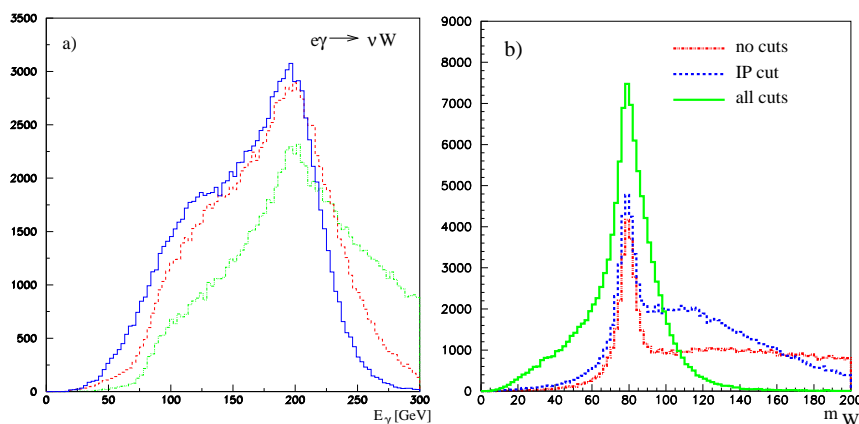


Figure 10. Reconstructed W-energy (a) and -mass (b) at the different levels of pileup rejection in the $e\gamma \rightarrow W\nu$ analysis for the parasitic mode.

The events are fitted using a Monte Carlo reweighting technique where Whizard [35] is used as a generator. In the fit the W production angle, the two decay angles and the energy are used. In addition to the triple gauge couplings a free normalisation constant is fitted, where the normalisation is constrained to unity with an assumed error on the efficiency and luminosity determination.

Table 2 summarises the results for different fit assumptions assuming one year of running. The precision on κ_γ depends mainly in the precision on the total cross section and thus on the assumed normalisation error. λ_γ has only little sensitivity to the normalisation but is more sensitive to pileup and background. The correlation between $\Delta\kappa_\gamma$ and $\Delta\lambda_\gamma$ is negligible in all cases.

Several sources of systematic errors have been considered. Assuming $\Delta\mathcal{L}/\mathcal{L} = 0.1\%$ the beam polarisation needs to be known to 0.1% in order that $\Delta\kappa_\gamma$ is not dominated by this error. At the same time the background has to be known to a precision of better than 3% in the real mode and 1% in the parasitic mode. λ_γ is basically not sensitive to both variations. Both coupling constants are not sensitive to realistic variations in the luminosity spectrum.

Table 2

Estimated statistical errors for κ_γ and λ_γ from $e\gamma \rightarrow W\nu$ for the real/parasitic $e\gamma$ mode with different assumptions for one year of running.

$\Delta\mathcal{L}$	1%	0.1%	0
without pileup and background			
$\Delta\kappa_\gamma \cdot 10^{-3}$	3.4/4.0	1.0/1.0	0.5/0.5
$\Delta\lambda_\gamma \cdot 10^{-4}$	4.9/5.5	4.5/5.2	4.5/5.1
with pileup no background			
$\Delta\kappa_\gamma \cdot 10^{-3}$	3.5/4.5	1.0/1.0	0.5/0.5
$\Delta\lambda_\gamma \cdot 10^{-4}$	5.2/6.7	4.9/6.4	4.9/6.4
with pileup and background			
$\Delta\kappa_\gamma \cdot 10^{-3}$	3.6/4.8	1.0/1.1	0.5/0.6
$\Delta\lambda_\gamma \cdot 10^{-4}$	5.2/7.0	4.9/6.7	4.9/6.7

2.3.2 Analysis of $\gamma\gamma \rightarrow W^+W^-$

A similar analysis has been performed for $\gamma\gamma \rightarrow W^+W^-$ using both angular momentum states $|J_z| = 0, 2$ [34]. The only relevant background for this channel is the process $\gamma\gamma \rightarrow q\bar{q}$ where four jets are produced from gluon radiation. Since there are always two W-bosons in the event, typically at low angles, angular cuts are not effective against pileup, which can thus only be rejected by the impact parameter cut. Events are selected by cuts on the reconstructed invariant mass of the W-bosons and the angle between the two jets belonging to one W in the centre of mass frame of the event. With these cuts an efficiency of $\sim 50\%$ and a purity of $\sim 80\%$ has been achieved for both J_z states.

The data have also been fitted with a Monte Carlo reweighting technique. In this case the fit has been done in six dimensions, the W-production angle, two decay angles per W and the WW centre of mass energy. Again the two anomalous couplings have been fitted together with a free but constrained normalisation factor. Table 3 summarises the results for the two angular momentum states for one year of running. Like in $e\gamma$ the sensitivity to κ_γ is determined by the cross section measurement while λ_γ is given by the shape of the events. Consequently λ_γ suffers more from the presence of pileup and background. λ_γ is determined better from $|J_z| = 2$ while for the same luminosity error $J_z = 0$ is more sensitive to κ_γ . However the luminosity can be determined much more precise in $|J_z| = 2$ so that this mode is the better one for both coupling constants.

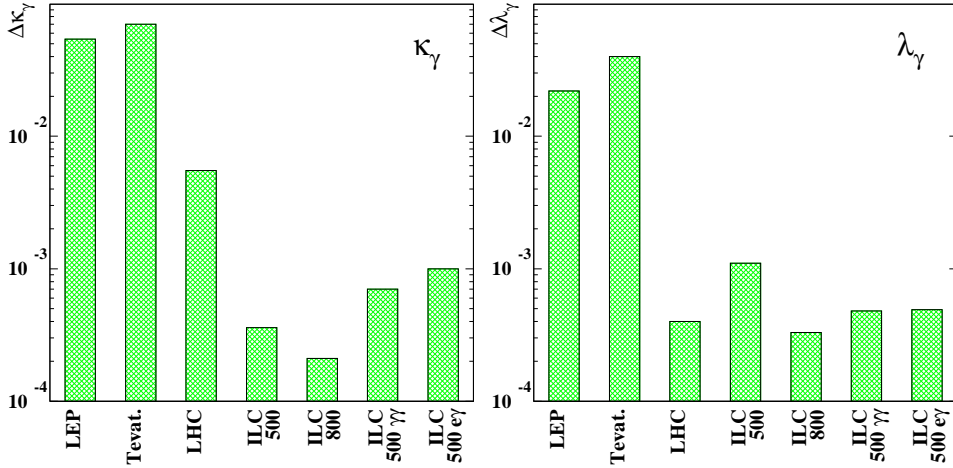
Figure 11 compares the precision of the fits to κ_γ and λ_γ for the different machines. For e^+e^- the results for the 5-parameter fit to $g_Z, \kappa_\gamma, \kappa_Z, \lambda_\gamma, \lambda_Z$ are shown. For κ_γ e^+e^- is clearly superior to $\gamma\gamma$ and $e\gamma$. For λ_γ the photon collider

Table 3

Estimated statistical errors for κ_γ and λ_γ from $\gamma\gamma \rightarrow WW$ for $J_z = 0/|J_z| = 2$ with different assumptions for one year of running.

$\Delta\mathcal{L}$	1%	0.1%	0
without pileup and background			
$\Delta\kappa_\gamma \cdot 10^{-4}$	19.9/29.9	5.5/6.2	2.6/3.7
$\Delta\lambda_\gamma \cdot 10^{-4}$	3.7/3.1	3.7/3.1	3.7/3.1
with pileup no background			
$\Delta\kappa_\gamma \cdot 10^{-4}$	26.9/37.4	5.8/6.8	3.0/4.6
$\Delta\lambda_\gamma \cdot 10^{-4}$	5.4/4.6	5.2/4.6	5.2/4.6
with pileup and background			
$\Delta\kappa_\gamma \cdot 10^{-4}$	27.8/37.8	5.9/7.0	3.1/4.8
$\Delta\lambda_\gamma \cdot 10^{-4}$	5.7/4.8	5.6/4.8	5.6/4.8

is better in both modes, however generator studies indicate that LHC could reach a similar accuracy.

Figure 11. Sensitivity to anomalous $WW\gamma$ couplings at different machines.

2.4 Supersymmetry

Supersymmetry (SUSY) is generally considered to be the best motivated extension of the Standard Model [36,37]. Therefore it will be shown in a few examples what a photon collider can do for SUSY. Since photons couple simply to charge the cross sections can be calculated without model dependence and the photon collider can thus be used to study decay properties of supersymmetric particles.

As few examples of analyses with supersymmetric particles, sleptons and charginos in the benchmark point SPS1a [38] and variants of this scenario, have been studied. This parameter-point assumes minimal SUGRA with mass unification at the GUT scale and relatively light superpartners. The masses and decay modes of the relevant superpartners are shown in table 4.

Table 4

Masses of the Higgses and light superpartners in the SPS1a scenario.

	m_{SPS1a}		m_{SPS1a}
h	111.6	H	399.6
A	399.1	H^\pm	407.1
$\tilde{\chi}_1^0$	97.03	$\tilde{\chi}_2^0$	182.9
$\tilde{\chi}_3^0$	349.2	$\tilde{\chi}_4^0$	370.3
$\tilde{\chi}_1^\pm$	182.3	$\tilde{\chi}_2^\pm$	370.6
\tilde{e}_1	144.9	\tilde{e}_2	204.2
$\tilde{\mu}_1$	144.9	$\tilde{\mu}_2$	204.2
$\tilde{\tau}_1$	135.5	$\tilde{\tau}_2$	207.9
$\tilde{\nu}_e$	188.2		

2.4.1 Slepton production in $\gamma\gamma$ collisions

In most models the $\tilde{\mu}_R$ decays only into $\mu\tilde{\chi}_1^0$ so that for $\tilde{\mu}_R$ -pair production probably no information on Supersymmetry breaking parameters can be obtained. Nevertheless this process has been simulated inside SPS1a [39]. The process is mainly characterised by an acoplanar muon pair in the detector. Below the $\tilde{\mu}_L$ production threshold the main background is W-pair production. The signal can be selected with an efficiency of 85% and a purity of 59% resulting in a precision on the cross section measurement of 1.6% in a month of running (100 fb^{-1}). This cross section precision can also be interpreted as a 0.8% precision of the branching ratio $BR(\tilde{\mu}_R \rightarrow \mu\tilde{\chi}_1^0)$ where it has to be assumed that possible other $\tilde{\mu}_R$ decays don't give any background to the selected channel.

In the SPS1a scenario the study of $\tilde{\mu}_L$ decays is much more interesting, since three decay channels are open $\tilde{\mu}_L \rightarrow \mu\tilde{\chi}_1^0$ (55%), $\tilde{\mu}_L \rightarrow \mu\tilde{\chi}_2^0$ (17%) and $\tilde{\mu}_L \rightarrow \nu_\mu\tilde{\chi}_1^\pm$ (28%). $\tilde{\mu}_L$ pair production has been simulated at $\sqrt{s_{\text{ee}}} = 600 \text{ GeV}$ where one expects $3 \cdot 10^4$ events in one year of running [39]. Figure 12 shows the muon momentum distribution from $\tilde{\mu}_L$ decays together with the expected background. For the signal one can see three distinct regions. At high momenta there are only muons from the $\tilde{\mu}_L \rightarrow \mu\tilde{\chi}_1^0$ decay, the muons at medium momenta are from the $\tilde{\mu}_L \rightarrow \mu\tilde{\chi}_2^0$ decay and the ones at low momenta are from

$\tilde{\chi}_2^0$ decays.

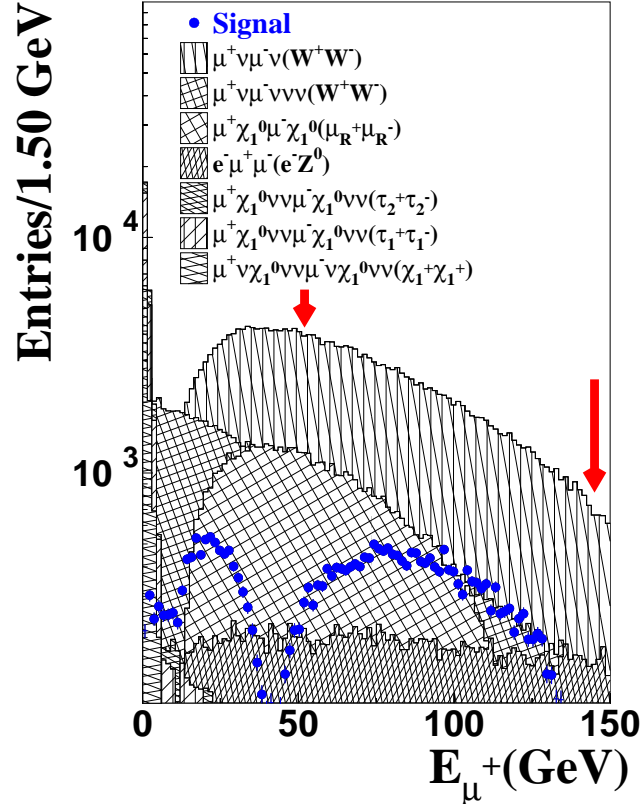


Figure 12. Momentum spectrum of from $\tilde{\mu}_L \rightarrow \mu X$ decays and from the relevant background processes.

Selecting the high momentum region one can with similar cuts as for the $\tilde{\mu}_R$ analysis measure the cross section $\gamma\gamma \rightarrow \tilde{\mu}_L + \tilde{\mu}_L^- \rightarrow \mu^+ \tilde{\chi}_1^0 \mu^- \tilde{\chi}_1^0$ with a precision of around 2% and the corresponding branching ratio $\text{BR}(\tilde{\mu}_L \rightarrow \mu \tilde{\chi}_1^0)$ with a precision of around 1%. This branching ratio should be sensitive to the mixing angles in the chargino and neutralino sector.

2.4.2 Chargino production in $\gamma\gamma$ collisions

A chargino can decay either into a W and a neutralino or, if kinematically allowed, into a slepton and the corresponding lepton³. The flavour composition of the leptons is non-trivial and depends on the SUSY-breaking parameters. Within SPS1a the $\tilde{\chi}_1^\pm$ decays almost exclusively into $\tilde{\tau}_1 \nu_\tau$, so that no meaningful branching ratio measurement is possible. Therefore for a simulation study m_0 has been changed to 130 GeV and $\tan\beta$ to 9. With these parameters the $\tilde{\chi}_1^\pm$ decays in 26% of the cases into $W \tilde{\chi}_1^0$ and in 73% into $\tilde{\tau}_1 \nu_\tau$. The process $\gamma\gamma \rightarrow \tilde{\chi}_1^+ \tilde{\chi}_1^-$ has been simulated with both charginos decaying into $W \tilde{\chi}_1^0$ and the W decaying hadronically. Details of the analysis can be found

³ Other decays like decays into virtual squarks are usually suppressed

in [40]. Assuming that the production cross section is known the event rate is proportional to $\text{BR}(\tilde{\chi}_1^\pm \rightarrow W\tilde{\chi}_1^0)^2$.

Because of the huge WW background an efficiency of 24% and a purity of 11% is possible at $\sqrt{s_{ee}} = 600 \text{ GeV}$, leading to a relative branching ratio error of 3.5%. To test the usefulness of this measurement it has been injected into the fit of the low energy SUSY breaking parameters with Fittino using the masses and cross sections from the LC/LHC study [41]. Due to the $\tilde{\chi}_1^\pm$ branching ratio measurements the precision on $\tan\beta$ and on the $\tilde{\tau}$ mixing parameter improve by a factor two to three. However up to now no decay related observables from e^+e^- are used in the fit.

2.4.3 Selectron production in $e\gamma \rightarrow \tilde{e}_R\tilde{\chi}_1^0$

If the mass difference $\tilde{e}_R\tilde{\chi}_1^0$ is large it is possible that the reaction $e^+e^- \rightarrow \tilde{e}_R^+\tilde{e}_R^-$ is not accessible while $e\gamma \rightarrow \tilde{e}_R\tilde{\chi}_1^0$ can be seen at the same e^-e^- centre of mass energy. In mSUGRA this happens e.g. if m_0 and $m_{1/2}$ are of approximately the same size. If this happens in mSUGRA the chargino and neutralino sector would be accessible in e^+e^- via $e^+e^- \rightarrow \tilde{\chi}_1^0\tilde{\chi}_2^0, \tilde{\chi}_2^0\tilde{\chi}_2^0, \tilde{\chi}_1^+\tilde{\chi}_1^-$ so that $m_{1/2}$ could be measured already there while m_0 can only be obtained from the $e\gamma$ mode. Without gauge unification it is also possible to adjust the parameters in a way that no visible SUSY signal is present in e^+e^- .

In most models the \tilde{e}_R decays dominantly into $e\tilde{\chi}_1^0$ so that if R-parity is conserved the experimental signal is a single electron in the detector. There are two irreducible background channels: $e\gamma \rightarrow W\nu$ with $W \rightarrow e\nu$ and $W \rightarrow \tau\nu \rightarrow e3\nu$ and $e\gamma \rightarrow eZ \rightarrow e\nu\bar{\nu}$. In most cases the lightest sfermion is the partner of the right-handed electron, so that the signal is enhanced using right-handed electron beams. This polarisation suppresses simultaneously the W-background which is present for left-handed electrons only. Also the Z-background is reduced slightly in this case.

Signal and background have been simulated using SHERPA [26] where the following SUSY parameters have been used:

$$\begin{aligned} m_0 &= 250 \text{ GeV} \\ m_{1/2} &= 250 \text{ GeV} \\ A &= 0 \\ \tan\beta &= 50 \\ \text{sign}(\mu) &= +1 \end{aligned}$$

resulting in

$$\begin{aligned}
m(\tilde{e}_R) &= 273 \text{ GeV} \\
m(\tilde{\chi}_1^0) &= 100 \text{ GeV} \\
m(\tilde{\chi}_2^0) &= 190 \text{ GeV} \\
m(\tilde{\chi}_1^\pm) &= 190 \text{ GeV}
\end{aligned}$$

with the \tilde{e}_R decaying almost exclusively into $e\tilde{\chi}_1^0$ [42]. With cuts in the electron energy and polar angle an efficiency of $\varepsilon = 71\%$ and a purity $p = 63\%$ can be reached allowing a 1% cross section measurement in one year of running. As shown in [16] the selectron and neutralino mass can be obtained from the two endpoints of the electron energy spectrum in case of monoenergetic beams. For the simulated parameter set the neutralino mass can be measured in e^+e^- running, so that one endpoint is sufficient to obtain the selectron mass. Because of the sharp upper edge of photon energy spectrum the lower endpoint is approximately preserved. The upper edge gets distorted by the dependence of the \tilde{e}_R -energy from its polar angle but can be reconstructed from the electron transverse momentum. It has been estimated that from the lower endpoint the selectron mass can be measured with a precision of 0.5%. The precision from the upper endpoint is significantly worse.

2.5 Luminosity Measurement

As for any collider, the luminosity at a $\gamma\gamma$ and $e\gamma$ collider has to be measured using gauge reactions with a large and well known cross section. Since the photon polarisation depends strongly on its energy, the luminosity spectrum has to be measured separately for the different polarisation states. A general discussion about the luminosity measurement at $\gamma\gamma$ and $e\gamma$ colliders can be found in [43].

A QED process involving only leptons is the ideal gauge process since it has basically no unproven physics assumptions involved. The process $\gamma\gamma \rightarrow e^+e^-, \mu^+\mu^-$ has a cross section of a few pb with realistic tracking cuts for a total $\gamma\gamma$ angular momentum of $|J_z| = 2$ [43]. This allows for a luminosity precision around 0.1% in one year of running. For $J_z = 0$ the cross section is suppressed by m^2/s because of helicity conservation and thus not usable for luminosity determination.

The process $\gamma\gamma \rightarrow \ell^+\ell^-\ell^+\ell^-$ has in principle a very large cross section independent from the beam polarisation. Unfortunately the leptons in this case are mostly at very low polar angle where they cannot be measured [44].

W-pair production has a very large cross section (~ 80 pb) for both polarisation states. However its size depends on the triple gauge couplings which must be assumed to use the process as a gauge process. If the gauge couplings

are measured in e^+e^- or $\gamma\gamma$ with $|J_z| = 2$, W-pair production can be used for a luminosity measurement in $J_z = 0$ with a precision better than 1%. This is largely sufficient for a possible measurement of heavy SUSY Higgses or superpartners.

The accurate measurement of the partial width $H \rightarrow \gamma\gamma$ for a light Standard Model like Higgs of course has to be done with $J_z = 0$. Its mass is either below the W-pair production threshold or the Higgs decays dominantly into a W-pair, so that W-pair production can never be used as a gauge process. A candidate gauge process here is $\gamma\gamma \rightarrow \ell^+\ell^-\gamma$. Because of the extra radiated photon the mass suppression does not apply and the cross section for monoenergetic beams is around 1 pb for $\sqrt{s} = 120$ GeV [45]. This allows to measure the luminosity to 1% in a mass window ± 2 GeV around the Higgs mass in one year of running using muons only. Figure 13 shows the energy spectrum of photons from the process $\gamma\gamma \rightarrow \ell^+\ell^-\gamma$ for $|J_z| = 2$ and $J = 0$. While for $|J_z| = 2$ the usual $1/E$ spectrum can be seen for $J = 0$ the cross section is actually rising with the photon energy.

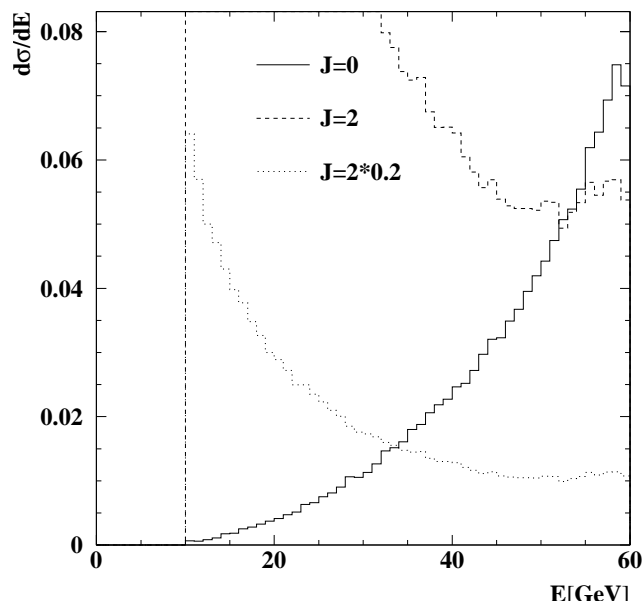


Figure 13. Cross section $\gamma\gamma \rightarrow \ell^+\ell^-\gamma$ for $|J_z| = 2$ and $J = 0$. The dotted line shows the $|J_z| = 2$ cross section multiplied by 0.2.

For $e\gamma$ running the situation concerning polarisation is slightly more complicated. For weak processes the electron coupling depends on the electron spin while all processes depend on the $e\gamma$ angular momentum so that in principle the luminosity for all four possible polarisation states needs to be known. On the other hand QED conserves parity so that with a QED process only the luminosity for a given $e\gamma$ angular momentum can be measured. Fortunately the electron and γ polarisation at high energies are quite high and the electron polarisation can be measured with high accuracy.

The cross section $e\gamma \rightarrow e\gamma$ is proportional to $1/(1 - \cos\theta)$ for $|J_z| = 1/2$ while it is proportional to $1 - \cos\theta$ for $|J_z| = 3/2$. In the real $e\gamma$ mode, where only one beam is converted there is thus a chance to get both components from the angular dependence. In the parasitic mode, where in general only $|\cos\theta|$ can be measured it seems difficult to identify the small $|J_z| = 3/2$ component. $e\gamma \rightarrow e^-e^+e^-$ has a measurable cross section within the detector independent from the beam polarisation and can be used to measure the $|J_z| = 3/2$ component once the $|J_z| = 1/2$ component is known [43].

The process $e\gamma \rightarrow W^-\nu$ is sensitive to left handed electrons only. Again the triple gauge couplings need to be known if the process should be used for luminosity determination

3 Technical Issues

The $\gamma\gamma$ collider imposes several technical challenges [2]. The most important one is certainly the laser system. In order to reach high conversion factors a laser power of $\mathcal{O}(10 \text{ J/pulse})$ and a spot size of $\mathcal{O}(10 \mu\text{m})$ is needed.

Due to the interaction with the laser the electron beam gets significantly disrupted. This requires a large crossing angle between the beams. Due to these two facts a large energy is deposited on the detector surface which potentially result in substantial background in the detector.

Another challenge is the beam dump. Photons cannot be deflected, so that the energy density at the dump is large. There will be a direct line of sight from the dump to the interaction point so that neutrons created in the dump can reach sensitive detectors.

Another problem is the feedback system. The disrupted beam can probably not be used for a fast feedback, since the low energy tail is too strongly deflected by the detector solenoid. A possible idea is to use low charge bunches between the main bunches [46]. A detailed study is needed to proof that this is possible.

3.1 The Laser Cavity

The production of 10 J laser pulses with a frequency of 10 kHz is difficult if not impossible by today's standards. But from the more than 10^{19} photons in a laser pulse only $\mathcal{O}(10^{10})$ are used per beam-laser interaction. This makes it natural to reuse a laser pulse many times. An optical ring resonator has been proposed for this purpose [47,48,49]. For this option a conceptual design has been developed [50], which is summarised below. The time between two

bunches at the ILC is about 3 ns, so that the total length of the cavity is approximately 100 m

3.1.1 Power enhancement within a passive optical cavity

Inside an optical ring resonator the circulating electric field directly after the input coupling mirror M_c is given by a superposition of the transmitted incoming electric field and a scaled replica of the circulating field that emerged from this coupling mirror at the previous round-trip.

On resonance the power enhancement factor A_q describes a monotonous increase of power after the cavity has been filled with q pulses:

$$A_q = (1 - R_c) \left[\frac{1 - \left(\sqrt{R_c V} \right)^q}{1 - \sqrt{R_c V}} \right]^2$$

R_c represents the intensity reflectivity of the coupling mirror and V the power loss factor for one round-trip.

If the reflectivity of the coupling mirror equals the loss factor V of the cavity, the maximum possible steady-state power enhancement factor of $A_\infty = 1/(1 - V)$ is obtained and all light is absorbed by the resonant cavity. This is known as impedance matching.

On resonance no power will be reflected from an impedance matched cavity in steady state. The reflected power can be used as an indicator for the alignment of the cavity in an automated control system.

3.1.2 Proposed design for an optical cavity

To maintain a sufficiently high photon density and hence a high conversion factor, the laser pulse must be focused at the Compton conversion point (CP). When operated at the inevitable high power level optical windows within the cavity would imply the risk of distortion of the circulating optical picosecond-pulse as a result of the non-vanishing B-integral [51,52]. The Compton-interaction requires therefore operation of the cavity in the vacuum of the accelerator.

Due to space limitations and to avoid vibrations any component of the optical cavity should preferably be positioned outside the environment of the particle detector, a few metres away from the laser focus. As a consequence of the

required tight optical focus and the large distance the cross section of the laser beam at the first mirror will increase to more than half a metre.

Compton conversion at each of the counter-propagating electron beams requires two ring cavities as exemplified by Fig. 14. They are interlaced without mutual interference. Their optical paths are enclosed within the associated

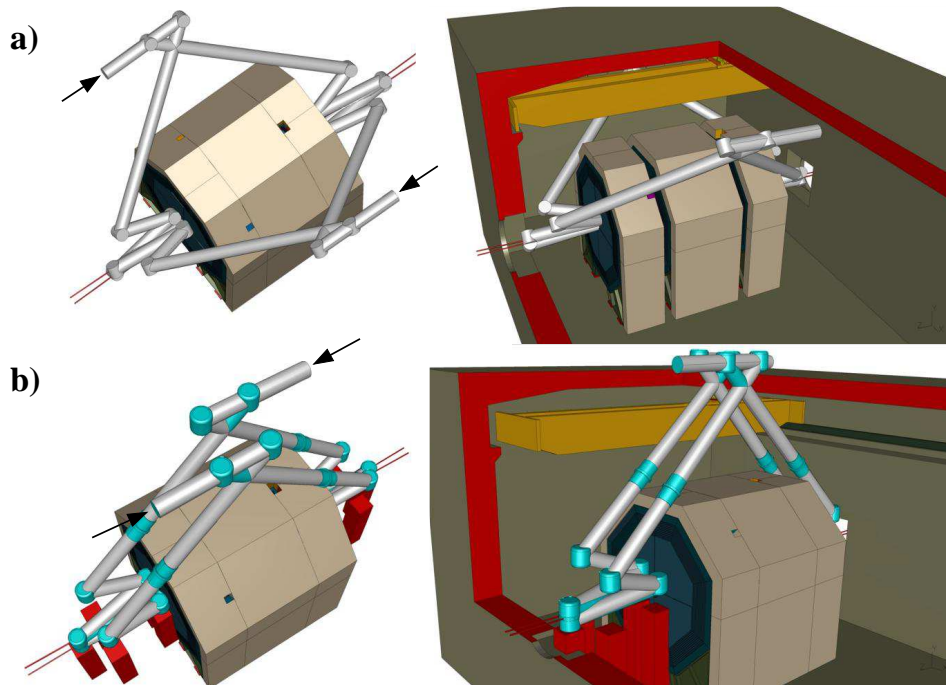


Figure 14. Schematic aerial view on two possible configurations for folding both optical cavities for the TESLA photon collider around the detector (*left*). Their respective placement in the experimental hall is also depicted (*right*). The laser beams are coupled into the cavity at positions marked by the arrows. The optical beam path is contained within the sketched pipes that preserve the vacuum. The high power lasers itself will be located in a separate hall above the detector (not shown). The thin lines traversing the detector represent the electron beam paths. A slight mutual vertical tilt between the cavities permits free passage of the particle beams. As a ruler: The detector extends 14.8 m along the electron path.

optical beam pipes which are needed to maintain the vacuum. For details see [50]. The focusing is accomplished by means of a reflective beam expander and a second, identical telescope is used for re-collimation. In addition, this introduces a moderate beam magnification of $\sqrt{3}$ for reduction of the beam size within the nearly collimated region of the cavity outside the detector.

The focal spot size at the CP and the influence of the finite diameter of the mirrors were calculated numerically [50]. Total correction of the aberrations introduced by the telescope mirrors was thereby assumed. The diameter of the final focusing concave mirrors determines the minimal collision angle α_l between the laser and the electron beam. It should be kept small for high yield

of photons. The major effect in reducing the size of the mirrors is a diffractive broadening of the focal spot size. The increased loss due to radiative energy that spills over the boundaries of the mirrors turned out to be much smaller. Figure 15 shows the broadening of the focal spot due to the final size of the focusing mirror as a function of the radius of this mirror.

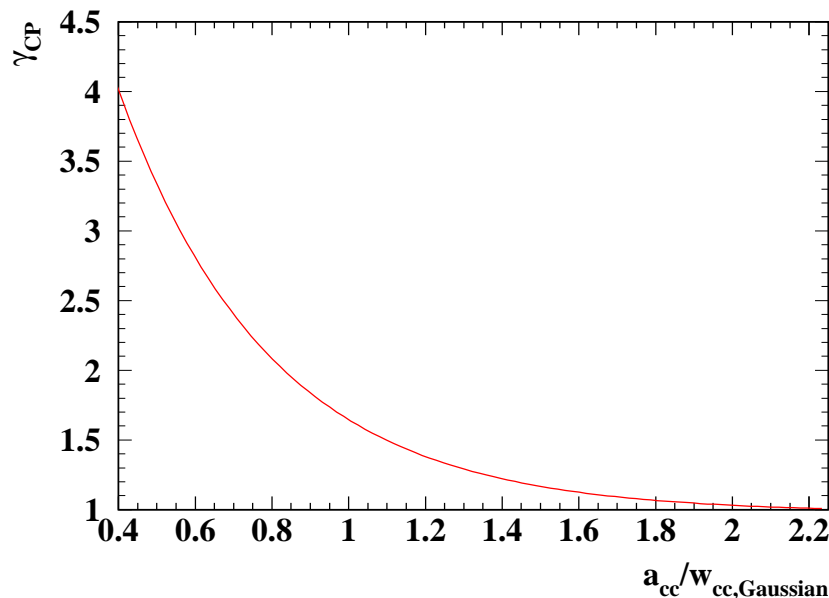


Figure 15. Broadening of the focal spot due to the final size of the focusing mirror as a function of the radius of this mirror. The x-axis shows the size of the mirror normalised to the radius of the beam ($1/e^2$ convention). The y-axis shows the size of the focus normalised to its value for infinite mirrors.

3.1.3 Laser-electron crossing angle

In order to calculate the laser-electron crossing angle α_l and to specify w_{CP} , diffraction broadening has to be taken into account. To optimise the yield of photons, the crossing angle α_l , the mirror diameter $2a_{cc}$, the waist size w_{CP} , the laser pulse energy E_{pulse} , as well as the laser pulse duration τ_{pulse} are all interdependent parameters. Their respective values were determined by a numerical optimisation process using the program CAIN [9] to calculate the yield. CAIN assumes that charged particles interact with a Gaussian optical beam. The centre-of-mass energy was set to 500 GeV. The aperture $2a_{cc}$ of the final focusing concave mirrors M_4 , M_5 at distance L_{image} from the conversion point CP in Fig. 16 sets an upper limit for the opening angle θ_{cc} of the laser cone that emerges from the beam waist:

$$\theta_{cc} = \frac{a_{cc}}{L_{image}} = \frac{a_{cc}}{w_{cc}} \theta_L \quad .$$

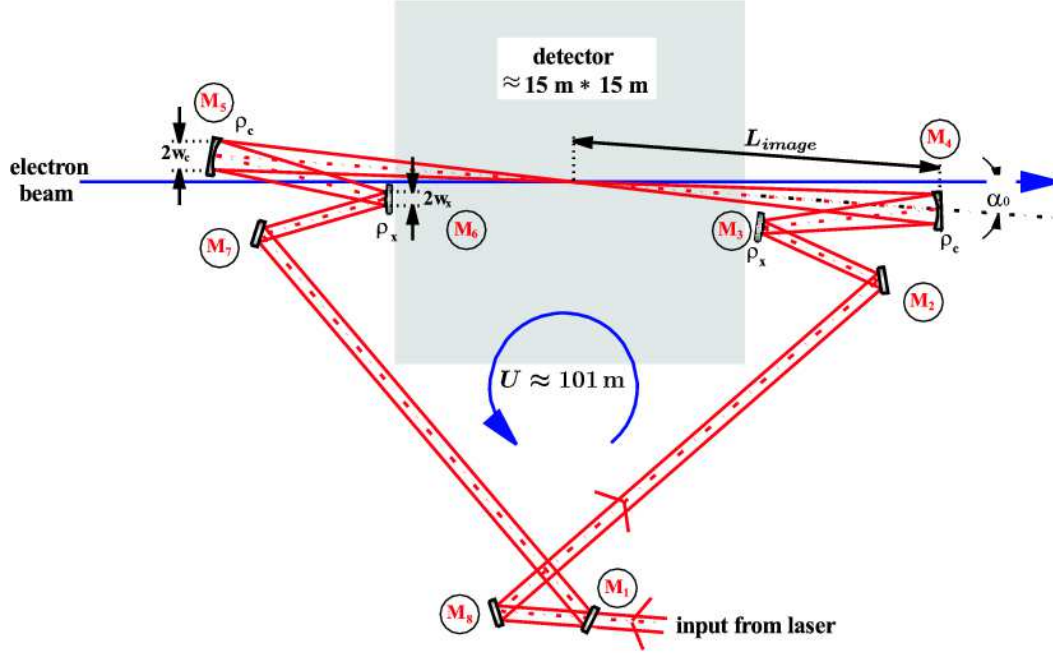


Figure 16. Geometry (to scale) of one of the identical plane cavity, comprising a beam magnification $\mu = w_c/w_x$. CP: Compton conversion point.

Replacing L_{image} by the far field divergence angle θ_L originating from a Gaussian beam waist w_0 results in the latter equation. w_{cc} represents the beam radius on each of the concave mirrors. If the electron beams cross each other in the horizontal ($x-z$) plane, the laser beams should run in the vertical ($y-z$) plane. To allow for an opening angle of the outgoing beampipe of 14 mrad and the finite size of the focusing quadrupole, it is assumed that the lower edge of the laser beampipe stays away from the horizontal plane by 17 mrad. If the quadrupole can be smaller a lower offset angle is possible allowing for a slightly smaller laser power or higher luminosity. The projection of the different pipes in the $x-y$ plane at the front face of the final quadrupole is shown in figure 17.

The crossing angle α_l is thus expressed as

$$\alpha_l = \frac{a_{cc}}{w_{cc}} \theta_L + \beta, \quad \beta = 17 \text{ mrad}.$$

This relation was encoded into CAIN via the optical Rayleigh length $z_R = \pi w_0^2/\lambda$ and the relation $\theta_L = w_0/z_R$ of Gaussian beams [53]. Instead of the Gaussian beam waist, the numerical value for the diffraction broadened waist $w_{CP} = \gamma w_{CP, Gaussian}$ has been used for w_0 . In the central part of the pulse in the diffraction broadened case the beam is well approximated by a diffraction limited Gaussian profile using the modified Rayleigh length. Fig. 18 shows the resulting luminosity as a function of the crossing angle α_l for different mirror sizes a_{cc}/w_{cc} and a laser pulse duration of $\tau_L = 3.5 \text{ ps}$ FWHM ($\sigma = 1.5 \text{ ps}$).

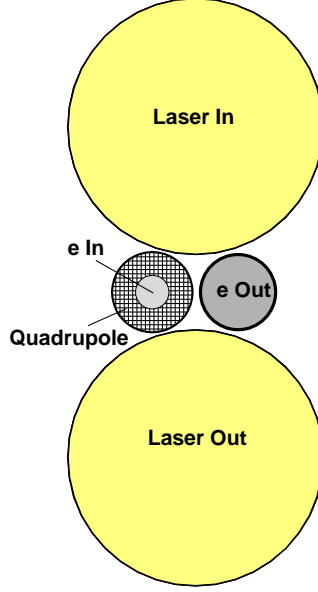


Figure 17. Arrangement of the laser- and beam-pipes at the front face of the final quadrupole ($z = \pm 3.8$ m).

In the examined range the luminosity rises with decreasing diameter of the mirrors. A value of $a_{cc}/w_{cc} = 0.75$ is therefore selected. An acceptable crossing angle is then $\alpha_l \approx 55$ mrad. This corresponds to $z_R(w_{CP}) \approx 0.63$ mm, a diffraction broadened beam waist of $w_{CP} \approx 14.3 \mu\text{m}$ ⁴ and a nominal Gaussian waist of $w_{CP, Gaussian} \approx 6.5 \mu\text{m}$.

A total luminosity⁵ of $\mathcal{L}(z > 0.8z_{max}) = 1.1 \cdot 10^{34} \text{ cm}^{-2}\text{s}^{-1}$ can be achieved for these parameters with a pulse energy of 9 J [54]. A non-linearity parameter $\xi^2 = 0.3$ can be maintained in accordance with reference [2], however the required laser power is 80% larger. In proportion to the laser pulse energy the required average laser power has also gone up to $9 \text{ J} \times 2820 \times 5 \text{ Hz} \approx 130 \text{ kW}$. All resulting parameters for the Compton interaction zone of a $\gamma\gamma$ -collider based on 250 GeV electron beams are compiled in Tab. 5.

3.1.4 Enhancement capability of the cavity

According to the results obtained in [50] all mirrors could have a diameter of about 120 cm. In this case cutoff occurs at approximately 75 % of the hypothetical Gaussian beam radius ($1/e^2$) at the final focusing mirror which represents the dominant aperture at which diffraction will occur.

⁴ w_{CP} is given in the $1/e^2$ convention, designating the radius that is defined by a drop of the intensity to $1/e^2 \approx 13.5$ % of its maximum value at the beam centre. Given in Gaussian σ its value is a factor two smaller.

⁵ Here z_{max} is defined as $z_{max} = x/(x+1+\xi^2)$ consistent with the definition in [2].

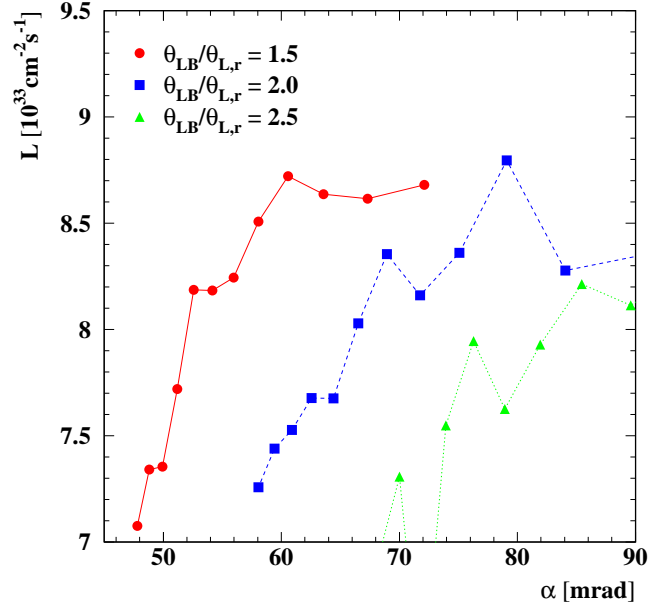


Figure 18. The $\gamma\gamma$ luminosity in the high energy part of the Compton spectrum as calculated using CAIN. It is plotted as a function of the laser-beam crossing angle α_l for different values of the steric opening angle Θ_{LB} of the concave mirror. It is given in units of the rms angular divergence $\Theta_{L,r}$ of the laser light in the focal point ($\Theta_{LB}/\Theta_{L,r} = 2a_{cc}/w_{cc,Gaussian}$). The high energy part was defined as $z > 0.8z_{max}$, whereas $z_{max} = x/(x+1)$, neglecting non-linearity effects.

Table 5

Optical parameters resulting from an optimisation of the $\gamma\gamma$ luminosity

laser pulse energy E_{pulse}	≈ 9.0 J
average laser power $\langle P_{laser} \rangle_t$	≈ 130 kW for one pass collisions at the TESLA bunch-structure
pulse duration τ_{pulse}	3.53 ps FWHM ($\sigma = 1.5$ ps)
Rayleigh length z_R	≈ 0.63 mm
beam waist w_{CP}	$\approx 14.3 \mu\text{m}$ ($1/e^2$) ($\sigma = 7.15 \mu\text{m}$)
laser- e^- crossing-angle α_l	≈ 56 mrad
normalised mirror-size a/w	0.75
laser wavelength λ	$1.064 \mu\text{m}$
nonlinearity parameter ζ^2	0.30
total luminosity $L_{\gamma\gamma}$	$1.05 \cdot 10^{34} \text{ cm}^{-2} \text{ s}^{-1}$

An estimated fractional power loss due to diffraction of roughly $LF_{\text{diff}} \geq 0.9998$ per round trip and a reflectivity of between $R_{HR} = 99.99\%$ and 99.95% for presently available standard mirror coatings would permit a steady-state

impedance matched power enhancement between 1100 and 270, for otherwise perfect conditions. The enhancement becomes the more sensitive against any impedance mismatch, the larger A_∞ is.

The optical energy fluence of $\approx 13 \text{ J/cm}^2$ is expected to be well below the damage threshold of mirror substrates and coatings. However, no data for trains of ps-pulses separated on nano- to microsecond time scales which accumulate to the stated fluence exist. For a final judgement an experimental study with a representative of the ILC bunch structure would be required.

3.1.5 *Effects of cavity misalignments*

Any misalignment of a mirror position and orientation generally results in displacement and broadening of the intra-cavity beam waist. According to our calculations, the displacement of the beam waist remains smaller than the Rayleigh length, i.e. the depth of the focus. This shift of the beam waist is hence negligible.

Maintaining the power enhancement factor e.g. above 90% of its optimum value A_∞ demands sub-nm precision for controlling the circumference. Technical solutions for such a precise length stabilisation are well-known [55]. Even more stringent restrictions are common in interferometrical detection of gravitational waves. For the latter case control loops for automatic alignment have been developed. Despite the different operation modes, the use of bursts of optical ps-pulses for the $\gamma\gamma$ collider and continuous-wave (cw) laser radiation in optical interferometers for gravitational waves, the cavity for the $\gamma\gamma$ -collider should benefit from that knowledge. In addition, adaptive optics appears to be essential for operation of such a cavity for the photon collider. It helps substantially to endure the development of a diffraction limited optical mode despite the expected thermal distortion due to absorption of a tiny fraction of the circulating optical power within optical coatings and the substrates of the cavity mirrors.

3.2 *Detector and Backgrounds*

Machine backgrounds at a linear collider are mainly coming from beam-beam effects in the interaction region [56]. There are several differences between an e^+e^- and a $\gamma\gamma$ collider: The electron beam gets disrupted in the electron-laser interaction with a disruption angle around 10 mrad. This precludes head on collision since the outgoing beam does no longer fit through the aperture of the final focusing quadrupole. The beam radius increases further due to the angle between the outgoing beam and the magnetic field of the detector solenoid. Figure 19 shows the angular spread of the outgoing electron beam directly

behind the interaction point and at $z = 2.8$ m. To limit the energy loss in the detector an opening angle of 14 mrad for the outgoing beampipe has been chosen. A crossing angle of 34 mrad had been adapted, as suggested in [2]. The front face of the final quadrupole is assumed to be $l^* = 3.8$ m away from the interaction point. With recent designs of small superconducting quadrupoles [10] this crossing angle or even a slightly smaller one should be possible.

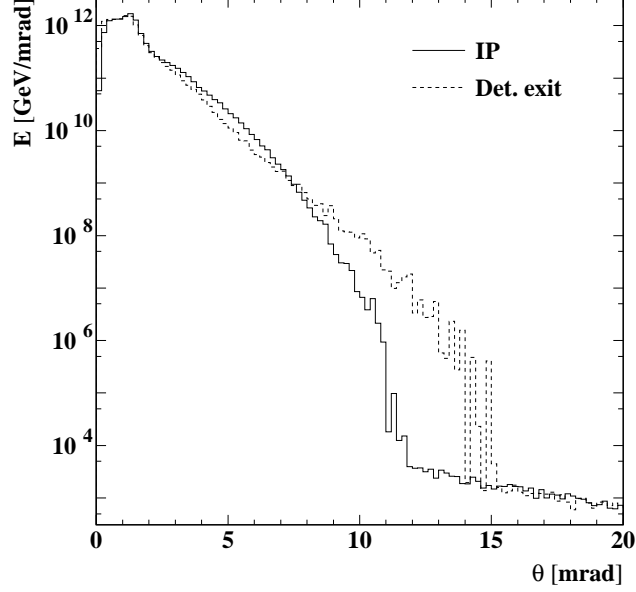


Figure 19. Energy weighted angular distribution of the outgoing electron beam directly behind the interaction point (solid) and at $z = 2.8$ m (dashed).

For simplicity, the detector is assumed to be identical to the e^+e^- detector described in [56] above polar angles of $\theta = 7^\circ$. Below this angle it has to be modified to accommodate the $\gamma\gamma$ specific equipment. The tracking system of the detector is shown in figure 20.

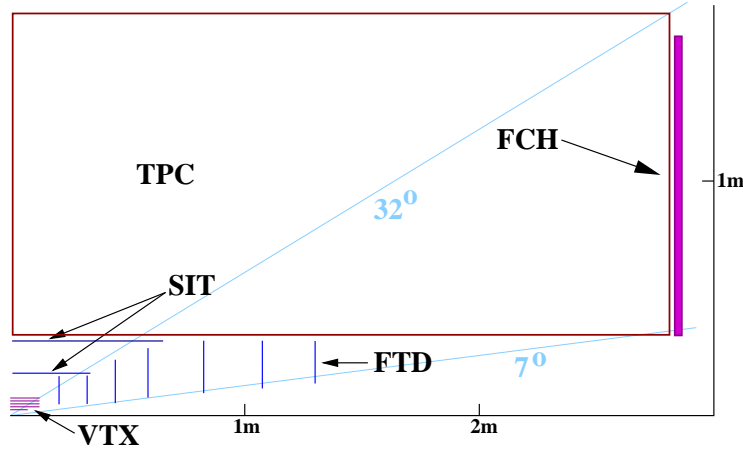


Figure 20. Tracking system of the TESLA TDR detector.

Detailed backgrounds have been simulated using CAIN [9]. For these simulations the incoherent particle-particle as well as the coherent particle-beam

interactions have been considered. The direct background at large angle is exclusively coming from incoherent e^+e^- pair creation. This background is significantly smaller than in the e^+e^- version of TESLA [56]. Another significant amount of background is coming from backscattering of particles. This background is potentially larger than in e^+e^- for several reasons. Because of the crossing angle the particles already hit the detector at a larger radius than in e^+e^- . Also because of the crossing angles the beams are not parallel to the solenoid, so that low momentum particles get swept out of the beampipe by the magnetic field. Low energy electrons of one bunch get deflected by the negative charge of the opposing bunch, while they are focused by the opposite charge in e^+e^- . Some electrons get deflected enough by the electron-laser interaction that they hit the detector or the inner side of the beampipe close to the detector.

Figure 21 shows the energy weighted angular distribution of particles and the energy distribution at $z = 2.8$ m, the front-face of the electromagnetic calorimeter. In total 40 TeV per bunch crossing are deposited on the front face of the mask from pair production at the IP. This is roughly the same energy as for the e^+e^- option described in [56]. Because of the large crossing angle, however, the backscattered particles are more difficult to capture by the masking system. There is also a danger that several hundred TeV of electrons hit the mask very close to the exit whole. These electrons stem from multiple interactions with the laser beam. They have a significantly larger energy than the pairs and contribute thus much less to the backscattering. If needed these particles can be suppressed by making the beampipe in the horizontal plane slightly larger.

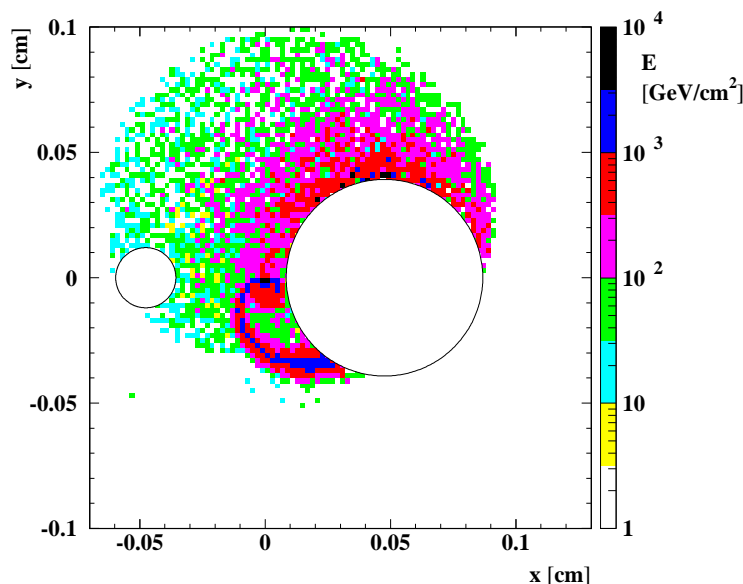


Figure 21. Energy deposition from one bunch crossing at $z = 2.8$ m, the front face of the ECAL.

The inner part of the detector had to be completely redesigned to house the pipes for the beam and the laser. To avoid scattering surfaces inside the detector the beampipe is identical to the e^+e^- case up to $z = 17$ cm followed by a conical part with opening angle 93 mrad up to $z = \pm 2.825$ m.

Only behind the front-face of the calorimeter the common beampipe splits into individual ones for the incoming and outgoing beams and lasers. To absorb backscattered particles the pipes are surrounded by a tungsten mask with pointing geometry and at thickness of 5 cm at $z = 2.8$ m.

Another mask of 5 cm thickness is put inside the beampipe where the space needed for the laser is left free. Since the background is not symmetric in the azimuthal angle the function of the mask is not deteriorated by this. The outer mask starts at $z=23$ cm to protect as much as possible of the detector, the inner mask starts at $z=1$ m because otherwise it receives too many direct hits from background particles created at the interaction point. The photon background in the TPC as a function of the z -coordinate where the photon enters the TPC is shown in fig. 22 with and without the inner mask. It is evident that the inner mask is needed to protect the TPC.

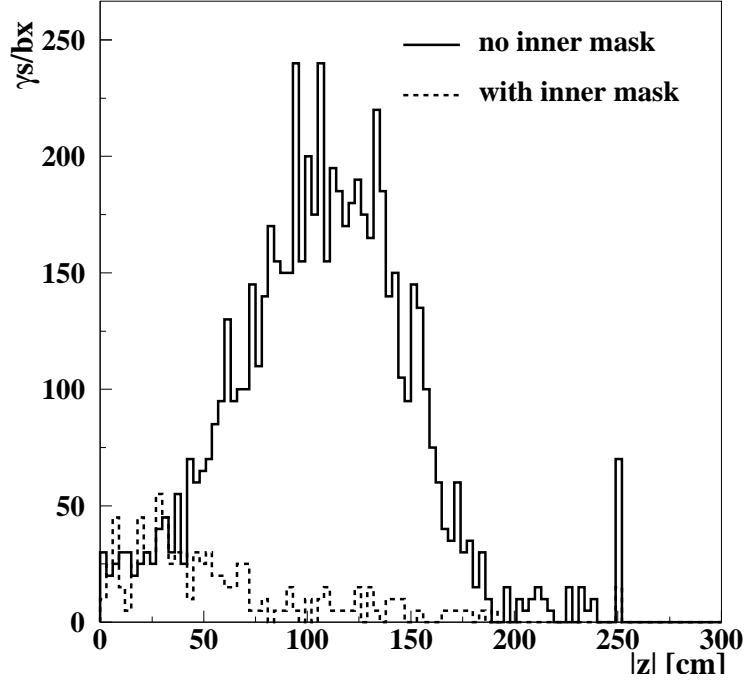


Figure 22. z -coordinate of photons entering the TPC.

Figure 23 shows the beampipe region in the $x - y$ and $x - z$ projection. This setup has been simulated using the TESLA simulation program BRAHMS [57] which is based on GEANT3 [58]. The detector is hermetic above $\theta = 7^\circ$. Inside the mask it should be possible to install some tagging devices for photon structure function measurements left and right of the beampipe (see fig. 17) where the background level is relatively low (fig. 19). In $e\gamma$ running it should

also be possible to replace the unused laser pipe at negative y by a tagging device.

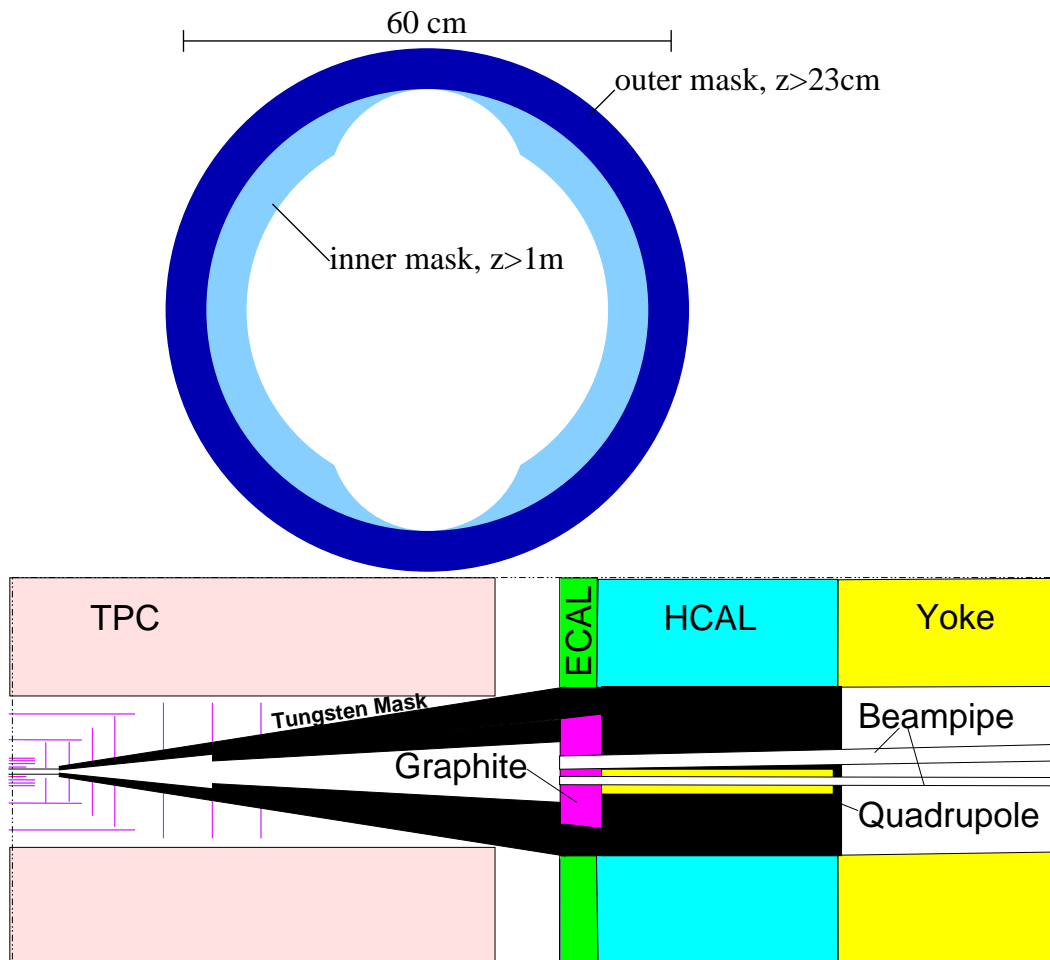


Figure 23. x-y projection at $z = 2.8\text{ m}$ (upper plot) and x-z projection of the inner region of the $\gamma\gamma$ -detector.

Figure 24 shows the background in the vertex detector separated into direct hits and hits from backscattering. The total number of hits in the different layers is very similar to e^+e^- , however in e^+e^- basically all hits are direct. In $\gamma\gamma$ the innermost layer of the vertex detector cannot be protected by the mask so that it receives a significant amount of backscattering. The background shown in figure 24 is only from incoherent processes at the interaction point. In addition a background of two times around 15 hits per bunch crossing and layer is present from low energy $\gamma\gamma \rightarrow q\bar{q}$ events, explained in section 2.1, and from backscattering from showers induced by electrons that loose exceptionally much energy in the interaction with the laser or by beamstrahlung. The latter process is very rare, but consist of relatively large showers, so that the fluctuations are large.

The number of photons passing the TPC is estimated to be 1800/bunch cross-

ing. Also this number is comparable to the e^+e^- case [56] and should be manageable.

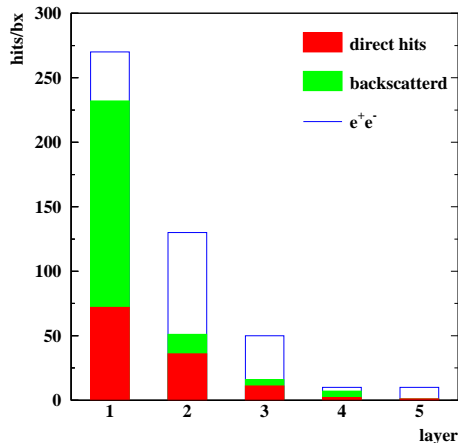


Figure 24. Hits in the microvertex detector from e^+e^- pairs created in the interaction region.

3.3 The Beamdump

Since photons cannot be deflected there has to be a direct line of sight from the interaction point to the beam dump. The standard ILC design uses a water dump at a distance of about 100 m from the detector. Such a dump has been simulated with Geant4 [59] using the physics list QGSP_HP and a cross section bias of 100. Cross checks have been done with LHEP_GN, QGSP_GN, and a cross section bias of one and consistent results have been found. For a neutron kinetic energy of $E_n > 15$ keV about 3.5 neutrons/BX/cm² have been found with this setup from the γ -beam only, corresponding to $5 \cdot 10^{11}$ neutrons/cm²/year. If the electron beam will be dumped in the same beam dump this number has to be doubled. Such a neutron flux will be a problem for a CCD vertex detector. Some ideas how to reduce the neutron flux exist [60], but there is no detailed design yet.

Another problem for the dump is the high energy density of the photon beam which would heat the water in the dump locally too much. Some ideas how to avoid this are also presented in [60].

4 Conclusions

Depending on the physics scenario, nature has chosen, a photon collider is an interesting complement to the e^+e^- baseline version of the ILC. The final

decision if a photon collider will be built, should only be taken when supporting results from LHC and e^+e^- running of the ILC are available.

From the technical side the greatest challenge is probably the laser system. A conceptual design for a resonant laser cavity has been shown which could reach a power enhancement factor around 100 and thus reduce the required laser power to an acceptable level.

The detector at a photon collider seems manageable. The region below a polar angle of 7° is completely taken by pipes and the masking system, but at larger angles a detector similar to e^+e^- can provide comparable performance.

Acknowledgements

This work profited from useful discussion with many people. In particular we wish to thank J. Böhme, J. Gronberg, W. Kilian, F. Krauss, A. Leuschner, N. Meyners, D. Miller, V. Telnov, N. Walker, I. Will, K. Zapfe and A. Zarnecki.

References

- [1] I. F. Ginzburg, G. L. Kotkin, V. G. Serbo and V. I. Telnov, JETP Lett. **34**, 491 (1981).
- [2] ECFA/DESY Photon Collider Working Group, B. Badelek *et al.*, TESLA Technical Design Report, Part VI, Chapter 1: Photon collider at TESLA, hep-ex/0108012, DESY-01-011E.
- [3] R. Brinkmann *et al.*, TESLA Technical design report. Part II: The accelerator, DESY-01-011B.
- [4] N. Walker, talk given at the ALPG and GDE workshop Snowmass, Colorado, August 2005,
http://alcp2005.colorado.edu:8080/alcp2005/program/bcd_review_Walker.ppt.
- [5] V. B. Berestetskii, E. M. Lifshitz and L. P. Pitaevskii, Quantum electrodynamics, Pergamon Press, Oxford, 1982.
- [6] I. F. Ginzburg, G. L. Kotkin and S. I. Polityko, Sov. J. Nucl. Phys. **37**, 222 (1983).
- [7] I. F. Ginzburg, S. I. Polityko and G. L. Kotkin, Yad. Fiz. **40**, 1495 (1984).
- [8] I. F. Ginzburg, G. L. Kotkin and S. I. Polityko, Phys. Atom. Nucl. **56**, 1487 (1993).

- [9] P. Chenand, T. Ohgaki, T. Takahashi, A. Spitkovsky and K. Yokoya, Nucl.Instr.Meth. **A397**, 458 (1997).
- [10] Y. Nosochkov *et al.*, Contributed to Particle Accelerator Conference (PAC 05), Knoxville, Tennessee, 16-20 May 2005.
- [11] D. Schulte, Study of electromagnetic and hadronic background in the interaction region of the tesla collider, TESLA 97-08.
- [12] V. Telnov, private communication.
- [13] T. Ohl, *Circe Version 2.0: Beam Spectra for Simulating Linear Collider and Photon Collider Physics*,
ftp://hepfix.ikp.physik.tu-darmstadt.de/pub/ohl/circe2/doc/manual.pdf.
- [14] A. Zarnecki, CompAZ: parametrization of the photon collider luminosity spectra, LC-TOOL-2002-007.
- [15] ECFA/DESY LC Physics Working Group, E. Accomando *et al.*, Phys. Rept. **299**, 1 (1998), [hep-ph/9705442].
- [16] ECFA/DESY LC Physics Working Group, J. A. Aguilar-Saavedra *et al.*, TESLA Technical Design Report Part III: Physics at an e^+e^- Linear Collider, hep-ph/0106315, DESY-01-011C.
- [17] E. Boos *et al.*, Nucl. Instrum. Meth. **A472**, 100 (2001), [hep-ph/0103090].
- [18] Particle Data Group, S. Eidelman *et al.*, Phys. Lett. **B592**, 1 (2004).
- [19] D. Schulte, private communication.
- [20] T. Ohgaki, T. Takahashi and I. Watanabe, Phys. Rev. **D56**, 1723 (1997), [hep-ph/9703301].
- [21] S. Söldner-Rembold and G. Jikia, Nucl. Instrum. Meth. **A472**, 133 (2001), [hep-ex/0101056].
- [22] P. Niezurawski, A. F. Zarnecki and M. Krawczyk, Acta Phys. Polon. **B34**, 177 (2003), [hep-ph/0208234].
- [23] P. Niezurawski, hep-ph/0507004.
- [24] M. Pohl and H. J. Schreiber, hep-ex/0206009.
- [25] T. Sjostrand, L. Lonnblad and S. Mrenna, hep-ph/0108264.
- [26] T. Gleisberg *et al.*, JHEP **02**, 056 (2004), [hep-ph/0311263].
- [27] K. Mönig and A. Rosca, submitted to Acta Phys. Polon.
- [28] K. Mönig and A. Rosca, in preparation.
- [29] S. Bethke, Z. Kunszt, D. E. Soper and W. J. Stirling, Nucl. Phys. **B370**, 310 (1992).
- [30] R. Hawkins, LC-PHSM-2000-021.

- [31] K. J. F. Gaemers and G. J. Gounaris, *Zeit. Phys.* **C1**, 259 (1979).
- [32] K. Hagiwara, R. D. Peccei, D. Zeppenfeld and K. Hikasa, *Nucl. Phys.* **B282**, 253 (1987).
- [33] K. Mönig and J. Sekaric, *Eur. Phys. J.* **C38**, 427 (2005), [hep-ex/0410011].
- [34] K. Mönig and J. Sekaric, hep-ex/0507050.
- [35] W. Kilian, LC-TOOL-2001-039.
- [36] H. P. Nilles, *Phys. Rept.* **110**, 1 (1984).
- [37] H. E. Haber and G. L. Kane, *Phys. Rept.* **117**, 75 (1985).
- [38] B. C. Allanach *et al.*, *Eur. Phys. J.* **C25**, 113 (2002), [hep-ph/0202233].
- [39] H. Nieto, in preparation.
- [40] G. Klämke and K. Mönig, *Eur. Phys. J.* **C42**, 261 (2005), [hep-ph/0503191].
- [41] P. Bechtle, K. Desch, W. Porod and P. Wienemann, hep-ph/0511006.
- [42] I. Alvarez Illan and K. Mönig, LC-PHSM-2005-002.
- [43] A. V. Pak, D. V. Pavluchenko, S. S. Petrosyan, V. G. Serbo and V. I. Telnov, hep-ex/0301037.
- [44] N. Arteaga, C. Carimalo, W. Da Silva and F. Kapusta, Fast luminosity measurement at gamma gamma collider using gamma gamma \rightarrow 4 leptons process, Prepared for International Conference on the Structure and Interactions of the Photon and 14th International Workshop on Photon-Photon Collisions (Photon 2001), Ascona, Switzerland, 2-7 Sep 2001.
- [45] V. Makarenko, K. Mönig and T. Shishkina, *Eur. Phys. J.* **C32**, Suppl1143 (2003), [hep-ph/0306135].
- [46] N. Walker, private communication.
- [47] V. I. Telnov, *Nucl. Phys. Proc. Suppl.* **82**, 359 (2000), [hep-ex/9908005].
- [48] V. I. Telnov, *Int. J. Mod. Phys.* **A15**, 2577 (2000), [hep-ex/0003024].
- [49] I. Will, T. Quast, H. Redlin and W. Sandner, *Nucl. Instrum. Meth.* **A472**, 79 (2001).
- [50] G. Klemz, K. Mönig and I. Will, physics/0507078.
- [51] A. E. Siegman, *Lasers* (Mill Valley: University Science Books, 1986, Chapter 10.2).
- [52] W. Koechner, *Solid-State Laser Engineering* (Springer Series in Optical Sciences, Vol.1, 1999, Chapter 4, 11).
- [53] A. E. Siegman, *Lasers* (Mill Valley: University Science Books, 1986, Chapter 18).

- [54] F. Bechtel, <http://www-zeuthen.desy.de/ILC/gammagamma/lumi-opt.ps.gz>.
- [55] R. Drever *et al.*, Appl. Phys. B **31**, 97 (1983).
- [56] G. Alexander *et al.*, TESLA Technical design report. Part IV: A detector for TESLA, DESY-01-011D.
- [57] T. Behnke *et al.*, BRAHMS: A Monte Carlo for a Detector at a 500/800 GeV Linear Collider, LC-TOOL-2001-005.
- [58] S. Giani *et al.*, GEANT detector description and simulation tool, CERN program library long writeup W5013.
- [59] GEANT4, S. Agostinelli *et al.*, Nucl. Instrum. Meth. **A506**, 250 (2003).
- [60] L. I. Shekhtman and V. I. Telnov, physics/0411253.